TECHNICAL MEMORANDUM

X-425

FREE-FLIGHT INVESTIGATION AT SUPERSONIC SPEEDS OF THE STABILITY AND DRAG OF A 79° CLIPPED DELTA BOOST-GLIDE CONFIGURATION INCLUDING AN ANALOG STUDY OF COUPLED MOTIONS DURING THE FLIGHT

By Sherwood Hoffman and Willard S. Blanchard, Jr.

Langley Research Center
Langley Field, Va.

NATIONAL AERONAUTICS AND SPACE ADMINISTRATION

WASHINGTON January 1961

NATIONAL AERONAUTICS AND SPACE ADMINISTRATION

TECHNICAL MEMORANDUM X-425

FREE-FLIGHT INVESTIGATION AT SUPERSONIC SPEEDS OF THE STABILITY AND DRAG OF A 79° CLIPPED DELTA BOOST-GLIDE CONFIGURATION INCLUDING AN ANALOG STUDY OF COUPLED MOTIONS DURING THE FLIGHT*

By Sherwood Hoffman and Willard S. Blanchard, Jr.

SUMMARY

A free-flight investigation was conducted at Mach numbers between 1.2 and 3.4 to determine the aerodynamic characteristics and motions of a rocket-boosted model of a simplified boost-glide hypersonic configuration. The model had a 79° clipped delta planform, sharp leading edges, a blunt base, and symmetry in two planes. The mass moment of inertia in roll was about 4 percent of the value in pitch or yaw.

The model was both statically and dynamically stable near Mach number 3 at small angles of attack and sideslip. A disturbance in pitch to an angle of attack of about 12° resulted in roll oscillations and reversals, and coupling of the longitudinal and lateral forces. An analog study, in which the equations of motion for five degrees of freedom were used, generally simulated the magnitudes and frequencies of the angular motions and showed that the rate of change of effective dihedral derivative with angle of attack was a necessary derivative for simulating the coupled motions at the altitude and velocity of the test.

Linearized theory gave reasonable predictions of the pressure drag and of the static and dynamic stability derivatives for oscillations of small amplitude.

---

*Title, Unclassified.

INTRODUCTION

The National Aeronautics and Space Administration is devoting considerable effort to the design of boost-glide vehicles for flight into space, reentry, and landing. Previous studies, such as references 1 and 2, indicate that the reentry phase of such a mission is feasible from both aerodynamic-heating and loading aspects with properly designed lifting configurations. Wind-tunnel tests have been made to determine the aerodynamic characteristics of promising boost-glide shapes, some
examples of which may be found in references 3 to 5 for lifting bodies, L
references 6 to 8 for all-wing vehicles, and reference 9 for wing-body 1
combinations. The results presented in the references show that low- 1
aspect-ratio configurations may experience significant rolling moments 8
due to aerodynamic coupling of their longitudinal and lateral forces 6
at angles of attack or sideslip. The resulting rolling motions may become pronounced because the mass is concentrated along the longitudinal axis and therefore the inertia in roll is very small compared with the inertias in pitch and yaw. Information on the motions and on the cross-coupling derivatives involved would be valuable to the designers of boost-glide configurations, especially with regard to controls.

A rocket-boosted model of a simplified hypersonic glider configuration has been flight-tested to determine its aerodynamic characteristics and motions during free flight at supersonic speeds. The model was representative of an all-wing boost-glide vehicle in that its leading edge was highly swept and the maximum thickness was at its blunt base. The configuration differed from some proposed boost-glide configurations, since the leading edge was fairly sharp instead of rounded and because it had symmetry in two planes.

The model was flight-tested at the NASA Wallops Station, through a range of Mach numbers decelerating from 3.4 to about 1.2 with corresponding Reynolds numbers, based on mean aerodynamic chord, ranging from 30×10^6 to about 2.5×10^6. Pulse rockets disturbed the model in the pitch plane during the flight and a ten-channel telemeter transmitted continuous acceleration and pressure data to ground receiving stations. The analysis includes the determination of stability derivatives from small-amplitude oscillations, comparisons with predictions from linearized theory, and an analog simulation study of the coupled motions during large-amplitude oscillations. A small model also was tested from a helium gun to determine the transonic drag of the configuration.

SYMBOLS

The basic data are presented with respect to the body-axis system shown in figure 1. The axes originated at the center-of-gravity position located at the 53.1-percent longitudinal station on the longitudinal axis of the rocket model, and corresponded to the 31.8-percent station of the mean aerodynamic chord.

$a_{L,cg}$	longitudinal acceleration of center of gravity, g units
$a_{L,Hi}$	longitudinal accelerometer reading, high range, positive in positive X direction, g units
$a_{L,Lo}$	longitudinal accelerometer reading, low range, positive in positive X direction, g units
$a_{N,cg}$	normal acceleration of center of gravity, g units
$a_{N,n}$	normal accelerometer reading in nose section, positive in negative Z direction, g units
$a_{N,t}$	normal accelerometer reading in tail section, positive in negative Z direction, g units
a_Y	lateral accelerometer reading, positive in positive Y direction, g units
$a_{Y,cg}$	lateral acceleration of center of gravity, g units
b	span, ft
$\bar{c}$	mean aerodynamic chord, ft
C_D	drag coefficient, $\frac{\text{Drag}}{q_\infty S}$
$C_{D,b}$	base-drag coefficient, based on S, $\left(\frac{p_b - p_\infty}{q_\infty}\right) \times \frac{S_b}{S} \times 144$
$C_{D,f}$	friction-drag coefficient, based on S
$C_{D,p}$	pressure-drag coefficient, based on S

C_L lift coefficient, $\frac{\text{Lift}}{q_\infty S}$

C_l rolling-moment coefficient, $\frac{\text{Rolling moment}}{q_\infty Sb}$

C_m pitching-moment coefficient, $\frac{\text{Pitching moment}}{q_\infty S\bar{c}}$

C_N normal-force coefficient, $\frac{\text{Normal force}}{q_\infty S}$

L1186

C_n yawing-moment coefficient, $\frac{\text{Yawing moment}}{q_\infty Sb}$

C_X axial-force coefficient, positive in positive X direction, $\frac{\text{Axial force}}{q_\infty S}$

C_Y lateral-force coefficient, $\frac{\text{Lateral force}}{q_\infty S}$

C_{L_α} lift-force coefficient derivative, $\frac{\partial C_L}{\partial \alpha}$, per radian

C_{l_β} effective dihedral derivative, $\frac{\partial C_L}{\partial \beta}$, per radian

$C_{l_{\beta_\alpha}}$ rate of change of effective dihedral derivative with angle of attack, $\frac{\partial C_{l_\beta}}{\partial \alpha}$, per square radian

C_{l_p} damping-in-roll derivative, $\frac{\partial C_l}{\partial \frac{pb}{2V}}$, per radian

C_{l_r} rate of change of rolling-moment coefficient with yawing angular velocity factor, $\frac{\partial C_l}{\partial \frac{rb}{2V}}$, per radian

C_{m_α}	static stability derivative, $\frac{\partial C_m}{\partial \alpha}$, per radian
$C_{m_{\dot\alpha}}$	rate of change of pitching-moment coefficient with rate of change of angle-of-attack factor, $\frac{\partial C_m}{\partial \frac{\dot\alpha \bar c}{2V}}$, per radian
C_{m_β}	rate of change of pitching-moment coefficient with angle of sideslip, $\frac{\partial C_m}{\partial \beta}$, per radian
C_{m_q}	rate of change of pitching-moment coefficient with pitching angular velocity factor, $\frac{\partial C_m}{\partial \frac{q\bar c}{2V}}$, per radian
C_{N_α}	normal-force coefficient derivative, $\frac{\partial C_N}{\partial \alpha}$, per radian
C_{n_β}	directional stability derivative, $\frac{\partial C_n}{\partial \beta}$, per radian
$C_{n_{\dot\beta}}$	rate of change of yawing-moment coefficient with rate of change of angle-of-sideslip factor, $\frac{\partial C_n}{\partial \frac{\dot\beta b}{2V}}$, per radian
C_{n_p}	rate of change of yawing-moment coefficient with rolling angular velocity factor, $\frac{\partial C_n}{\partial \frac{pb}{2V}}$, per radian
C_{n_r}	rate of change of yawing-moment coefficient with yawing angular velocity factor, $\frac{\partial C_n}{\partial \frac{rb}{2V}}$, per radian

C_{Y_β} lateral-force coefficient derivative, $\frac{\partial C_Y}{\partial \beta}$, per radian

C_{Y_r} rate of change of side-force coefficient with angular velocity factor in yaw, $\frac{\partial C_Y}{\partial \frac{rb}{2V}}$, per radian

g acceleration due to gravity, 32.2 ft/sec^2

h altitude, ft

I_X, I_Y, I_Z moments of inertia in roll, pitch, and yaw about the X, Y, and Z axes, respectively, slug-ft^2

M free-stream Mach number

m mass, W/g, slugs

P period of short-period oscillation, sec

p,q,r angular velocity in roll, pitch, and yaw, radians/sec

$\dot{p},\dot{q},\dot{r}$ angular accelerations in roll, pitch, and yaw, radians/sec^2

p_b base pressure, lb/sq in.

p_∞ free-stream static pressure, lb/sq in.

q_∞ free-stream dynamic pressure, lb/sq ft

R Reynolds number, based on $\bar{c}$

S planform area, sq ft

S_b base area (including fins), sq ft

$T_{1/2}$ time for a transient oscillation to damp to one-half amplitude, sec

t time, sec

V free-stream velocity, ft/sec

W weight, lb

X,Y,Z	body-axis system, ft
x,y,z	distances from center of gravity, measured along X, Y, and Z axes, ft
α	angle of attack, radians
$\dot{\alpha}$	rate of change of angle of attack with time, $\frac{\partial\alpha}{\partial t}$, radians/sec
β	angle of sideslip, radians, or $\sqrt{M^2 - 1}$
$\dot{\beta}$	rate of change of angle of sideslip with time, $\frac{\partial\beta}{\partial t}$, radians/sec
γ	angle between flight path and horizontal, deg

MODELS AND INSTRUMENTATION

Drawings of the two models tested are presented in figure 2. The larger model (fig. 2(a)) was designed to be boosted by rockets whereas the smaller one (fig. 2(b)) was scaled down to permit it to be propelled from a 6-inch helium gun. Longitudinal distances shown are measured from the "theoretical" nose tip, which is 0.66 inch ahead of the actual nose. Photographs of the models are shown in figures 3 and 4. Physical characteristics of the rocket model are presented in table I. The dimensions of the small helium-gun model were 0.181 of those of the rocket model. The weight of the small model was 1.128 pounds and the center of gravity was located at the 42.5-percent station measured from the theoretical tip. The thin, pointed nose tip was strengthened with a small nose sting as is shown in figures 2(b) and 4.

The configuration had mirror symmetry in the horizontal and vertical planes, sharp leading edges, and a blunt trailing edge. The planform was a 78.87° clipped delta wing with streamwise tips, aspect ratio of 0.54, and taper ratio of 0.191. The side view consisted of a 4° half-angle triangular forebody, a flat afterbody, and a maximum thickness of 7.65 percent of the total length. All the surfaces were planar. The resulting body cross sections normal to the longitudinal axis were diamond-shaped from the nose to about 55 percent of the body length, hexagonal from the 55-percent station to about the 80-percent station, and octagonal from the 80-percent station to the trailing edge or base. The fins, which were located in the vertical plane of symmetry, had a

sweepback angle of 76° along the leading edge, a taper ratio of 0.33, an unswept trailing edge, and 7.67° total-angle wedge airfoil sections.

A ten-channel telemeter was installed in the rocket model and included the following instruments: high-range and low-range longitudinal accelerometers, normal accelerometers located near the center of gravity and in the rear of the model, a transverse accelerometer, angular accelerometers measuring pitching and yawing accelerations, roll-rate gyro, total pressure pickup and base pressure pickup. The base pressure was averaged over the semispan of the blunt trailing edge with a manifolded tube as is shown in figures 2(a) and 3(b). The locations of the instruments with respect to the center of gravity are given in table II.

L
1
1
8
6

TESTS

A photograph showing the rocket model and booster on the launcher at the NASA Wallops Station is presented as figure 5. The booster consisted of an Honest John for the first stage and a Nike for the second stage. A small rocket motor was installed in the base of the model (see fig. 2(a)) and was programed to separate the model from the second stage after Nike burnout. The calculated relative deceleration of the burned-out Nike and separated model, based on drag-to-weight ratios, was very small and indicated the possibility of collision after separation. Two $3\frac{1}{4}$-inch aircraft rocket motors were therefore employed to increase the Nike deceleration after the model and booster were separated. These motors were mounted on the forward end of the Nike (fig. 5) with their nozzles facing upstream at a 20° cant angle with respect to the booster center line. The nozzles were plugged to protect the grain and igniters from aerodynamic heating during the booster phases of flight. The model was disturbed only in pitch by 27-pound-second pulse rockets (burning time 0.05 second) approximately 5 seconds and 15 seconds after separation from the booster. Calculations indicated that each pulse rocket would pitch the model to an angle of attack of about 12°. The locations of the pulse rockets are shown in figure 2(a).

Flight-path data were obtained by tracking the model with the AN/FPS-16 tracking radar, the NASA modified SCR-584 tracking radar, and the Reeves modified SCR-584 radar. Atmospheric conditions were obtained from a rawinsonde balloon that was released just prior to the test. Mach number and dynamic pressure were determined from the total-pressure measurements on the model and the ambient pressures and temperatures at corresponding altitudes along the flight path.

The range of flight for which the data were reduced varied between Mach number 3.4 at an altitude of 35,000 feet to Mach number 1.2 at an altitude of about 68,000 feet as shown in figure 6. The uncertainties in the aerodynamic coefficients were inversely proportional to the free-stream dynamic pressure q_∞ and varied from a small amount at $M = 3.4$ and $q_\infty = 4{,}000$ lb/sq ft to a fairly large percentage of the coefficients near $M = 1.2$ and $q_\infty = 100$ lb/sq ft. The corresponding Reynolds numbers, based on $\bar{c}$, varied from 30×10^6 to about 2.5×10^6 as shown in figure 7.

Telemetered data, static pressure, dynamic pressure, and Mach number for three time intervals of the test are presented in figure 8. The points were machine plotted from magnetic-tape records and show occasional scatter points due to noise. The time interval between 29.7 seconds and 30.6 seconds, figure 8(a), shows that the model was disturbed by the booster at separation $(M \approx 3.4)$ and experienced small-amplitude sinusoidal oscillations in pitch $\dot{q}$ and yaw $\dot{r}$. The roll rate p was essentially constant and less than 2 radians per second. When the first pulse rocket fired (near $M = 2.8$), the angle of attack increased rapidly and then the model motions became coupled. The resulting roll rates initially exceeded the range (about ±30 radians per second) of the gyro. The intervals from 40.8 seconds to 41.7 seconds $(M \approx 2.3)$ and from 42.2 seconds to 43.1 seconds $(M \approx 2.2)$ show the on-scale measurements after the first pulse. (See figs. 8(b) and 8(c).) The accelerations and motions are nonlinear and coupled. The model oscillated in roll to the right and then experienced two roll reversals in the time interval from 40.8 seconds to 43.1 seconds. In general, the roll-rate oscillations following both pulses were unsteady and varied from positive oscillations to roll reversals and to negative oscillations.

The helium-gun model covered a Mach number range from 1.2 to 0.7 with corresponding Reynolds numbers (based on $\bar{c}$) varying from 6×10^6 to about 3.5×10^6 as shown in figure 7. Velocity, trajectory, and atmospheric data were measured by the CW Doppler velocimeter, the NASA modified SCR-584 tracking radar, and a rawinsonde balloon, respectively.

ANALYSIS

Total Force and Moment Data

The total force coefficients were determined from the instantaneous values of translatory acceleration of the center of gravity obtained by the method described in appendix A. The following relationships were used to compute the force coefficients:

$$-C_X = \frac{W}{q_\infty S} a_{L,cg} \tag{1}$$

$$C_N = \frac{W}{q_\infty S} a_{N,cg} \tag{2}$$

$$C_Y = \frac{W}{q_\infty S} a_{Y,cg} \tag{3}$$

The helium-gun model was tested at zero lift and had no instrumentation. The drag coefficients were determined from the flight-path angle, free-stream conditions, and decelerations obtained by a differentiation of the velocity-time curve from the CW Doppler velocimeter by use of the following relationship:

$$C_D = -\frac{W}{g q_\infty S}\left(\frac{dV}{dt} + g \sin \gamma\right) \tag{4}$$

The total pitching-moment, yawing-moment, and rolling-moment coefficients for the rocket model were computed from the instantaneous values of angular acceleration and angular velocity with the following expressions:

$$C_m = \frac{I_Y \dot{q}}{q_\infty S \bar{c}} + \frac{\left(I_X - I_Z\right) pr}{q_\infty S \bar{c}} \tag{5}$$

$$C_n = \frac{I_Z \dot{r}}{q_\infty S b} + \frac{\left(I_Y - I_X\right) pq}{q_\infty S b} \tag{6}$$

$$C_l = \frac{I_X \dot{p}}{q_\infty S b} + \frac{\left(I_Z - I_Y\right) qr}{q_\infty S b} \tag{7}$$

It should be noted that the values of the product-of-inertia terms were zero because the principal axis coincided with the longitudinal axis of the model. The values of the gyroscopic reaction terms became large when the model roll rates were large. Values for q and r were determined by integrating $\dot{q}$ and $\dot{r}$ over small time intervals and for $\dot{p}$ by differentiating the time-history records of p. The curves of q and r were assumed to be centered about zero to determine their magnitudes and signs through several cycles.

Small-Disturbance Analysis

The small-disturbance data near $M = 3.4$, shortly after the model separated from the booster, have been analyzed separately in the pitch plane and in the yaw plane by assuming two degrees of freedom. As was noted earlier, the roll rate near $M = 3.4$ was very small and practically constant. The values of C_{m_α} at $\alpha = 0$ and C_{n_β} at $\beta = 0$ were computed from the average period and time-to-damp to one-half amplitude of the transient oscillations in each plane by the following relationships:

$$C_{m_\alpha} = -\frac{4\pi^2 I_Y}{q_\infty S\bar{c}}\left[\frac{1}{P^2} + \frac{1}{4\pi^2}\left(\frac{0.693}{T_{1/2}}\right)^2\right] \tag{8}$$

$$C_{n_\beta} = \frac{4\pi^2 I_Z}{q_\infty Sb}\left[\frac{1}{P^2} + \frac{1}{4\pi^2}\left(\frac{0.693}{T_{1/2}}\right)^2\right] \tag{9}$$

and the corresponding values of C_{N_α} and C_{Y_β} were computed from

$$C_{N_\alpha} = \left(\frac{\Delta C_N}{\Delta C_m}\right)C_{m_\alpha} \tag{10}$$

$$C_{Y_\beta} = \left(\frac{\Delta C_Y}{\Delta C_n}\right)C_{n_\beta}$$

The rotary damping derivatives were calculated as follows:

$$C_{m_q} + C_{m_{\dot{\alpha}}} = -\frac{2I_Y}{\bar{c}^2}\left(\frac{1.386V}{q_\infty ST_{1/2}} - \frac{32.2}{W}C_{N_\alpha}\right) \tag{11}$$

$$C_{n_r} - C_{n_{\dot{\beta}}} = -\frac{2I_Z}{b^2}\left(\frac{1.386V}{q_\infty ST_{1/2}} + \frac{32.2}{W}C_{Y_\beta}\right) \tag{12}$$

Simulation of Coupled Motions

A simulation study of the coupled motions near Mach number 2 was made using the equations of motion for five degrees of freedom. The equation associated with the drag force was omitted since the velocity of the model was nearly constant through the time intervals studied. The cross-product inertia terms have been omitted from the equations since the

principal axis coincided with the body axis. The equations of motion were written for the body-axis system and are given in appendix B. A highly simplified motion study using three degrees of freedom also was made and the equations used are included in appendix B.

RESULTS AND DISCUSSION

The stability derivatives and drag coefficients referred to in the following sections are for the conditions of zero angle of attack and zero angle of sideslip, except where noted.

L1186

Longitudinal Stability

The variations of normal-force coefficient, pitching-moment coefficient, and axial-force coefficients with time near Mach number 3.4 are presented in figures 9(a), 9(b), and 9(c). The corresponding variations of C_m with C_N are given in figure 10. The oscillations are sinusoidal about a trim normal force of zero (due to model symmetry), damp with time, and have an averaged period of 0.175 second. The average slope $\left(\Delta C_m/\Delta C_N\right)$ in figure 10 indicates that the static margin was -0.124 and the center of pressure was located at the 61.7-percent longitudinal station measured from the theoretical tip of the configuration.

The time-to-damp to one-half amplitude $T_{1/2}$ was obtained by plotting the peak amplitudes of the transient oscillations of C_N and $\dot{q}$ against time on semilog paper as is shown in figure 11. The log decrement of the peak amplitudes was linear and $T_{1/2}$ was 0.62 second. The resulting values of C_{m_α} and C_{N_α} were computed to be -0.104 and 0.837, respectively. The amplitude of the pitching oscillations, based on these values, varied within $\pm 0.4^\circ$.

The static stability derivatives are compared in figure 12 with those from linearized theory (refs. 10 and 11) for thin, sweptback, tapered wings at $M = 3.4$ and with wind-tunnel data (ref. 9) at $M = 2.01$ and 1.41. The agreement with linearized theory is good and the variation of C_{N_α} and C_{m_α} with Mach number is as would be expected for low-aspect-ratio wings.

The sum of the rotary damping derivatives in pitch $C_{m_q} + C_{m_{\dot{\alpha}}}$ at $M = 3.4$, as determined by equation (11) was -0.077. In comparison, linearized theory (refs. 11 and 12) predicted a value of about -0.4. In a free-flight test of a 67.5° sweptback arrow wing (ref. 13) the

damping in pitch also was lower than the theoretical value at $M = 1.8$. It should be noted that these magnitudes are small and that the accuracy of measuring $C_{m_q} + C_{m_{\dot{\alpha}}}$ may be poor because they were obtained from the difference of two numbers having the same order of magnitude (eq. (11)).

Directional Stability

The variations of side-force coefficient and yawing-moment coefficient with time near $M = 3.4$ are presented in figures 13(a) and 13(b) and the corresponding variation of C_n with C_Y is given in figure 14. The yawing oscillations were sinusoidal, damped with time, and had a linear variation of the log decrement of the envelope of the transient oscillations (fig. 15). The rolling moment during this time interval is shown in figure 13(c) to be practically zero.

The data show an average yawing period of 0.270 second, $T_{1/2}$ equal to 1.16 seconds, static directional stability $\left(\Delta C_n/\Delta C_Y\right)$ of -0.65, and a center of pressure in yaw at the 73.8-percent longitudinal station from the theoretical nose tip of the configuration. The resulting values of C_{n_β} and C_{Y_β} were 0.098 and -0.151, respectively, and the amplitude of the yawing oscillation varied within $\pm 1.2^\circ$. The static directional stability is compared with theory at $M = 3.4$ and wind-tunnel data (ref. 9) at $M = 2.01$ and $M = 1.41$ in figure 16. The same theoretical methods that were used in pitch were employed with the exception that the derivatives for the body alone and vertical fins alone were calculated separately and then summed. The theoretical values of C_{Y_β} and C_{n_β} are somewhat higher than the test values and this may be due, partly, to the omission of interference calculations between the fins and body.

The sum of the measured rotary damping derivatives $C_{n_r} - C_{n_{\dot{\beta}}}$ from equation (12) was -0.652 at $M = 3.4$. The theoretical damping due to the vertical fins alone was -0.69.

Drag

The variations of total-drag coefficient and base-drag coefficient with Mach number at approximately zero angle of attack and angle of sideslip for the rocket model, helium-gun model, and for the geometrically similar wind-tunnel model (ref. 9) are presented in figure 17. Since α and β were not measured in flight, the values of C_D for the rocket model (at $\alpha \cong \beta \cong 0$) were taken as those values corresponding to $\sqrt{C_N^2 + C_Y^2}$ nearly zero. The drag for the helium-gun model is an

average drag about the zero-attitude condition since it is probable that the model was disturbed slightly upon ejection from the gun and oscillated through small angles.

Good agreement was obtained in C_D and $C_{D,b}$ for the rocket model and wind-tunnel model at supersonic speeds. The agreement shown in figure 17(a) between data for the rocket model and for the smaller helium-gun model near $M = 1.2$ is poor; and the general level of the drag curve from the smaller model appears to be lower in comparison. Part of this difference may be explained by the different test Reynolds numbers and
their effect on the friction drag. Computed $C_{D,f}$ curves using average L
Reynolds numbers and turbulent-friction coefficients for flat plates 1
(ref. 14) are presented in figure 17(a). If transition is assumed to 1
occur at the 20-percent longitudinal station of each flight model, the 8
friction drag curves would be changed only a negligible amount, since 6
the wetted area affected is small compared with the total wetted area. The remaining difference in total drag levels appears to be due to the effect of Reynolds number on the base drags and experimental accuracy. The test Reynolds number (fig. 7) of all the models below Mach number 2 varied between 6×10^6 and 2×10^6; and according to reference 15, the Reynolds numbers were in a critical range for transition. Reference 15 also shows that the base pressures and base drags of blunt-base bodies may vary significantly at these Reynolds numbers depending on whether the boundary layer is fully laminar, fully turbulent, or under transition.

The base-drag coefficients obtained from the tests and from the semiempirical method of reference 16 for two-dimensional airfoils are compared in figure 17(b). The semiempirical method is restricted to an all-turbulent boundary layer at supersonic speeds and requires an analogy between the base pressures and peak pressure rise associated with separation of the boundary layer. The comparison indicates that the base drag of the model was essentially two dimensional and that the boundary layer was turbulent for Mach numbers from about 2 to 3.4. At Mach numbers less than 2 the two-dimensional airfoils have significantly higher base drags than the rocket model drag. This result suggests that the boundary layer on the model was not fully turbulent at the lower Mach numbers and Reynolds numbers.

Figure 18 presents a comparison of the pressure drags from the rocket models, from linearized wing theory, and from supersonic area-rule theory. The theoretical pressure drag from wing theory (ref. 17) includes the sum of the wing drag with tip effects, fin drag, and interference drag between the wing and fins for subsonic leading-edge conditions. The area-rule pressure drag was determined in the manner described in reference 18 with the assumption that a polyhedron (having the same normal cross section as the base) extended downstream from the base to infinity in order to apply

the theory. The Fourier series solutions employed for the computations of the area-rule drag were convergent.

The linearized wing-theory pressure drag was in closer agreement with the experimental pressure drag than the area-rule drag through most of the Mach number range. Although the magnitudes are small, the area-rule drag is significantly lower than that from the wing theory. In comparison, reference 18 shows nearly perfect agreement for the two theories for relatively blunt cones with large bases.

Coupled Motions

Typical time-history variations of the aerodynamic coefficients and cross plots of C_N against C_Y near Mach numbers of 2.3 and 1.8 are presented in figures 19 and 20, respectively. The curves defined by the data points are generally cyclic but not sinusoidal. It is clearly indicated that the motions are coupled, the damping in pitch and yaw is very poor, and the roll is oscillatory. The cross plots of C_N against C_Y in figures 19(g) and 20(g) are not representative of the relative motion in pitch and yaw (as they would be for a body having roll symmetry) since C_{N_α} is much higher than C_{Y_β} for the configuration.

The cross-hatched areas in figure 21 summarize the variations of the rolling rates of the model through the Mach number range. The large variations in roll-rate amplitude started near $M = 2.8$ when the first pulse rocket disturbed the model. The irregular pattern of positive and negative roll oscillations was not changed significantly when the second pulse rocket fired. Also shown in figure 21 are the divergence boundaries for steady roll, which were determined in the manner described in reference 19. It appears that the model rolling velocities are oscillating past the unstable regions.

Simulation of Coupled Motions

The simulation studies were conducted by use of equations of appendix B near Mach number 2 by using static stability derivatives from wind-tunnel tests and the free-stream conditions of the flight tests. The moment derivatives from reference 9 were recomputed about the model center of gravity. The pitch damping derivatives C_{m_q} and $C_{m_{\dot{\alpha}}}$ were initially calculated from linearized theory (refs. 11 and 12), but these values were lowered when they produced too much damping. The damping in yaw $\left(C_{n_r}\right.$ and $\left.C_{n_{\dot{\beta}}}\right)$ also were calculated, in a manner similar to that for pitch, with the assumption that all the damping was due to the vertical fins. The derivatives for C_{l_p} were estimated from reference 10,

and C_{l_r} and C_{n_p} were estimated from lifting-line theory. The values used for all the stability derivatives are listed in table III. It should be noted that two slopes were employed to approximate the nonlinear variations of C_{Y_β} and C_{n_β} with β, and $C_{l_{\beta_\alpha}}$ with α. The initial values for p, $\dot{r}$, and $\dot{q}$ were obtained from the flight records; the initial values of $\dot{p}$, r, and q were computed from flight data; and, the initial values of α and β were estimated to satisfy the equations of motion.

Consecutive analog runs showed that the simulated motions would not repeat exactly for identical initial conditions. The angular velocities and their frequencies were similar to those from the test and exhibited the type of oscillatory motions shown in figure 22(a). Small variations in the stability derivatives and use of other sets of initial conditions did not provide repeatability. The nonrepeatability appears to be due to the sensitivity of the equations, with the inputs used, to small computer errors of the analog. These small computer errors may be compared to spurious disturbances during the flight and, in this case, are partly responsible for the realistic simulation of the free-flight motions.

L 1 1 8 6

The flight variations of p, $\dot{r}$, and $\dot{q}$ with time are shown in figure 22(a) for comparison with three successive analog runs (initial conditions in table IV) in figures 22(b), 22(c), and 22(d). The first two runs simulate the roll data in magnitude and in the sequence of rolling oscillations and reversals. The third run differs mainly over the latter half of the run where positive roll oscillations follow the second roll reversal. The peak amplitudes and the frequencies of $\dot{q}$ and $\dot{r}$ were predicted by the equations but their variations with time were somewhat different from those of the test. The analog results also indicate that the ranges of α and β were less than ±0.2 radian (about 12°) as the rolling velocities oscillated past the divergence boundaries (fig. 17) for steady roll rates.

Several analog runs were made to determine the effect of $C_{l_{\beta_\alpha}}$ on the rolling motions. Oscillatory roll rates were obtained for all values between -0.1 and -1.2. Positive values of 0.1 and 0.2 resulted in damping of the initial roll rates to very small rates. These runs showed also that the rolling motions of the model could not be simulated without the $C_{l_{\beta_\alpha}}$ term in the equations of motion.

In order to isolate the effect of $C_{l_{\beta_\alpha}}$ on the motions, a simplified three-degree-of-freedom study was made by using equations (B6), (B7), and (B8) of appendix B. All stability derivatives, terms involving q and r, and gyroscopic reaction terms were dropped from equations (B1) to (B5), except $C_{l_{\beta_\alpha}}$ and the angular products βp and αp. The

simplified equations represent a mass distribution and flight condition (near $M = 2$ in the present case) for which such factors as $q_\infty S/mV$, $q_\infty S\bar{c}/I_Y$, $q_\infty S\bar{c}^2/2VI_Y$, and so on, may be considered negligible with regard to the $q_\infty Sb/I_X$ factor. The angular velocities q and r also were assumed to be zero to simplify the equations.

Figure 23 shows the typical variations of p, α, β, and $\dot{p}$ with time for the simplified equations using the initial conditions of table V and $C_{l_{\beta_\alpha}} = -0.82$. It can be seen that the rolling oscillations, reversals, and magnitudes are similar to those of the test in figure 22(a). As in the case of the five-degree-of-freedom study, this run also did not repeat exactly, showing that the simplified equations with the inputs used were sensitive to the small analog errors. Higher initial roll rates resulted in repeatable runs with oscillatory roll rates of higher frequency about the input value and no roll reversals; lower initial roll rates gave repeatable oscillations of lower frequency about zero roll velocity. It appears, therefore, that the input conditions which simulated the roll reversals of the test were also the critical input values for the simplified equations and for the equations used in the five-degree-of-freedom study. Comparisons of α and β from the simplified equations (fig. 23) with their corresponding values from the five-degree-of-freedom study (figs. 22(b) to 22(c)) show agreement in their peak amplitudes and frequencies. It is evident that the coupled motions, their frequencies and amplitudes, were highly dependent on the variation of the effective dihedral derivative with angle of attack, the relatively low roll inertia compared with the pitching and yawing inertias, and the altitude and velocity of the test.

L
1
1
8
6

CONCLUDING REMARKS

An investigation was conducted to determine the aerodynamic characteristics of a boost-glide type of hypersonic glider configuration at supersonic speeds. The configuration had a 79° clipped delta planform, sharp leading edges, a blunt base, and symmetry in two planes. The mass distribution was concentrated along the longitudinal axis and the inertia in roll was about 4 percent of the pitch or yawing inertias. The test covered a free-flight Mach number range from 3.4 to about 1.2.

The model was both statically and dynamically stable in pitch and yaw at small angles of attack and sideslip near Mach number 3. When the model was pitched to an angle of attack of about 12°, the configuration oscillated in pitch, roll, and yaw, indicating coupling of the longitudinal and lateral forces. An analog study near Mach number 2 generally simulated the magnitudes and frequencies of the angular motions and roll reversals, and showed that the rate of change of effective dihedral derivative with

angle of attack was a necessary derivative for simulating the coupled motions at the altitude and velocity of the test.

Linearized theory gave reasonable predictions of the static and dynamic stability derivatives for small angles of attack and yaw at Mach number 3.4. The pressure drag determined from linearized wing theory, including interference effects, was in closer agreement with the measured pressure drag than the pressure drag from area-rule theory through most of the Mach number range. The data indicate that the base drag was approximately two dimensional at the higher Mach numbers and
Reynolds numbers of the test. L
1
1
Langley Research Center, 8
National Aeronautics and Space Administration, 6
Langley Field, Va., September 9, 1960.

APPENDIX A

ACCELEROMETER CORRECTIONS

Linear accelerometers which are not mounted on the center of gravity measure not only the translatory accelerations but also the accelerations due to angular velocities and angular accelerations. Since the linear accelerometers in the model were off the center of gravity, it was necessary to subtract the rotational accelerations from the measured accelerations to obtain the translatory accelerations along the three axes. The following equations were used:

L1186

$$a_{L,cg} = a_{L,Lo} + \frac{1}{g}\left[x_{a_{L,Lo}}(q^2 + r^2) + y_{a_{L,Lo}}(\dot{r} - pq) - z_{a_{L,Lo}}(\dot{q} + pr)\right] \tag{A1}$$

$$a_{Y,cg} = a_Y + \frac{1}{g}\left[y_{a_Y}(r^2 + p^2) + z_{a_Y}(\dot{p} - qr) - x_{a_Y}(\dot{r} + pq)\right] \tag{A2}$$

$$a_{N,cg} = a_{N,n} + \frac{1}{g}\left[-z_{a_{N,n}}(p^2 + q^2) - x_{a_{N,n}}(\dot{q} - pr) + y_{a_{N,n}}(\dot{p} + qr)\right] \tag{A3}$$

where the distances x, y, and z from the center of gravity to the individual accelerometers are given in table II and are identified in these equations with subscripts indicating the accelerations measured. The corrections for $a_{L,Hi}$ and $a_{N,t}$ were made with expressions similar to equations (A1) and (A3). The variations of $\dot{q}$, $\dot{r}$, and p were measured directly from the angular accelerometers and the roll gyro, and required no corrections. The variations of q and r were obtained by integration of $\dot{q}$ and $\dot{r}$ over several cycles and by assuming that they varied symmetrically about zero values. The angular acceleration in roll $\dot{p}$ was obtained by differentiating the variations of p with t.

The values of $a_{L,Lo}$ and $a_{N,n}$ were used for determining $a_{L,cg}$ and $a_{N,cg}$ throughout most of the flight. The values of $a_{L,Hi}$ were used only at the higher Mach numbers where the deceleration was greater than the range of $a_{L,Lo}$; and $a_{N,t}$ served only as a check on $a_{N,cg}$.

APPENDIX B

EQUATIONS OF MOTION

The equations of motion used for the five-degree-of-freedom analog study are as follows:

$$\dot{\alpha} = q - \beta p - \frac{q_\infty S}{mV}\left(C_{L_\alpha}\alpha\right) \tag{B1}$$

L
1
1
8
6

$$\dot{\beta} = -r + \alpha p + \frac{q_\infty S}{mV}\left(C_{Y_\beta}\beta\right) \tag{B2}$$

$$\dot{p} = \left(\frac{I_Y - I_Z}{I_X}\right)qr + \frac{q_\infty Sb}{I_X}\left(C_{l_\beta}\beta + C_{l_{\beta\alpha}}\beta\alpha\right) + \frac{q_\infty Sb^2}{2VI_X}\left(C_{l_p}p + C_{l_r}r\right) \tag{B3}$$

$$\dot{q} = \left(\frac{I_Z - I_X}{I_Y}\right)pr + \frac{q_\infty S\bar{c}}{I_Y}\left(C_{m_\alpha}\alpha\right) + \frac{q_\infty S\bar{c}^2}{2VI_Y}\left(C_{m_q}q + C_{m_{\dot{\alpha}}}\dot{\alpha}\right) \tag{B4}$$

$$\dot{r} = \left(\frac{I_X - I_Y}{I_Z}\right)pq + \frac{q_\infty Sb}{I_Z}\left(C_{n_\beta}\beta\right) + \frac{q_\infty Sb^2}{2VI_Z}\left(C_{n_r}r + C_{n_{\dot{\beta}}}\dot{\beta} + C_{n_p}p\right) \tag{B5}$$

All gravity terms, as well as certain aerodynamic terms such as C_{m_β} and C_{Y_r}, have been omitted from equations (B1) to (B5). In the calculations it was assumed that $\dot{\beta} = -r$ in equation (B5); thus a slight simplification in the last term is possible. All the product-of-inertia terms were zero since the principal axis was coincident with the longitudinal axis.

The equations for the simplified analog study with three degrees of freedom are as follows:

$$\dot{\alpha} = -\beta p \tag{B6}$$

$$\dot{\beta} = \alpha p \tag{B7}$$

$$\dot{p} = \frac{q_\infty Sb}{I_X}\left(C_{l_{\beta\alpha}}\beta\alpha\right) \tag{B8}$$

REFERENCES

1. Allen, H. Julian, and Eggers A. J., Jr.: A Study of the Motion and Aerodynamic Heating of Ballistic Missiles Entering the Earth's Atmosphere at High Supersonic Speeds. NACA Rep. 1381, 1958. (Supersedes NACA TN 4047.)

2. Eggers, Alfred J., Jr., Allen, H. Julian, and Neice, Stanford E.: A Comparative Analysis of the Performance of Long-Range Hypervelocity Vehicles. NACA Rep. 1382, 1958. (Supersedes NACA TN 4046.)

3. Lange, Roy H.: Exploratory Investigation at a Mach Number of 5.20 of the Longitudinal Aerodynamic Characteristics of Flat-Bottom Bodies. NACA RM L56E30, 1956.

4. Ridyard, Herbert W.: The Aerodynamic Characteristics of Two Series of Lifting Bodies at Mach Number 6.86. NACA RM L54C15, 1954.

5. Paulson, John W.: Low-Speed Static Stability and Control Characteristics of a Model of a Right Triangular Pyramid Reentry Configuration. NASA MEMO 4-11-59L. 1959.

6. Robinson, Ross B., and Spearman, M. Leroy: Stability and Control Characteristics at a Mach Number of 1.89 of a Lightweight Glider Reentry Configuration. NASA TM X-276, 1960.

7. Shanks, Robert E.: Investigation of the Low-Subsonic Flight Characteristics of a Model of an All-Wing Hypersonic Boost-Glide Configuration Having Very High Sweep. NASA TN D-369, 1960.

8. Arabian, Donald D.: Investigation of the Rolling Stability Derivatives of Two Hypersonic Gliders of Parabolic Plan Form at High Subsonic Speeds. NASA TM X-268, 1960.

9. Foster, Gerald V.: Static Stability Characteristics of a Series of Hypersonic Boost-Glide Configurations at Mach Numbers of 1.41 and 2.01. NASA TM X-167, 1959.

10. Malvestuto, Frank S., Jr., Margolis, Kenneth, and Ribner, Herbert S.: Theoretical Lift and Damping in Roll at Supersonic Speeds of Thin Sweptback Tapered Wings With Streamwise Tips, Subsonic Leading Edges, and Supersonic Trailing Edges. NACA Rep. 970, 1950. (Supersedes NACA TN 1860.

11. Malvestuto, Frank S., Jr., and Hoover, Dorothy M.: Lift and Pitching Derivatives of Thin Sweptback Tapered Wings With Streamwise Tips and Subsonic Leading Edges at Supersonic Speeds. NACA TN 2294, 1951.

12. Malvestuto, Frank S., Jr., and Hoover, Dorothy M.: Supersonic Lift and Pitching Moment of Thin Sweptback Tapered Wings Produced by Constant Vertical Acceleration - Subsonic Leading Edges and Supersonic Trailing Edges. NACA TN 2315, 1951.

13. Gillespie, Warren, Jr.: Supersonic Aerodynamic Characteristics of a Low-Drag Aircraft Configuration Having an Arrow Wing of Aspect Ratio 1.86 and a Body of Fineness Ratio 20. NACA RM L57A25, 1957.

14. Van Driest, E. R.: Turbulent Boundary Layer in Compressible Fluids. Jour. Aero. Sci., vol. 18, no. 3, Mar. 1951, pp. 145-160, 216.

15. Kurzweg, H. H.: Interrelationship Between Boundary Layer and Base Pressure. Jour. Aero. Sci., vol. 18, no. 11, Nov. 1951, pp. 743-748.

16. Love, Eugene S.: Base Pressure at Supersonic Speeds on Two-Dimensional Airfoils and on Bodies of Revolution With and Without Fins Having Turbulent Boundary Layers. NACA TN 3819, 1957. (Supersedes NACA RM L53C02.)

17. Ferri, Antonio: Elements of Aerodynamics of Supersonic Flows. The Macmillan Co., 1949, pp. 292-349.

18. Nelson, Robert L., and Welsh, Clement J.: Some Examples of the Applications of the Transonic and Supersonic Area Rules to the Prediction of Wave Drag. NACA RM L56D11, 1957.

19. Sternfield, Leonard: A Simplified Method for Approximating the Transient Motion in Angles of Attack and Sideslip During a Constant Rolling Maneuver. NACA Rep. 1344, 1958. (Supersedes NACA RM L56F04.)

L
1
1
8
6

TABLE I

PHYSICAL CHARACTERISTICS OF ROCKET MODEL

L 1 1 8 6

Wing:	
Planform area, sq ft	5.86
Base area, sq ft	0.64
Span, ft	1.77
Aspect ratio	0.54
Root chord (model length to theoretical tip), ft	5.56
Mean aerodynamic chord, ft	3.83
Sweepback angle of leading edge, deg	78.87
Dihedral, deg	0
Thickness ratio	0.077
Taper ratio	0.191
Vertical tail:	
Planform area (2 fins exposed), sq ft	0.36
Base area (2 fins exposed), sq ft	0.05
Span (total), ft	0.85
Aspect ratio (exposed)	0.50
Sweepback angle of leading edge, deg	76.0
Wedge angle (total), deg	7.67
Taper ratio (exposed)	0.33
Mass characteristics:	
Weight, lb	108.0
Center-of-gravity position, rearward from theoretical tip in percent of total length	53.1
Moment of inertia in pitch, I_Y, slug-ft^2	6.93
Moment of inertia in yaw, I_Z, slug-ft^2	7.24
Moment of inertia in roll, I_X, slug-ft^2	0.27
Products of inertia, slug-ft^2	0

TABLE II

LOCATION OF INSTRUMENTS

Instrument	Distance from c.g.		
	x, ft	y, ft	z, ft
Longitudinal accelerometer for $a_{L,Hi}$	0.28	0.04	0
Longitudinal accelerometer for $a_{L,Lo}$	.28	-.04	0
Normal accelerometer for $a_{N,n}$	.075	0	0.082
Normal accelerometer for $a_{N,t}$	-2.118	.114	.059
Transverse accelerometer for a_Y	.431	-.033	0
Angular accelerometer in pitch for $\dot{q}$	-.144	-.064	0
Angular accelerometer in yaw for $\dot{r}$	.075	0	-.071
Roll-rate gyro for p	-.406	0	0
Total pressure pickup	Nose tip		
Base pressure pickup	Manifolded tube on base center line		

L
1
1
8
6

TABLE III

VALUES OF AERODYNAMIC DERIVATIVES USED IN EQUATIONS OF MOTION

C_{L_α}	1.0
C_{m_α}	-0.12
C_{m_q}	-0.05
$C_{m_{\dot{\alpha}}}$	-0.01
C_{Y_β}:	
For $0 < \beta < 0.5$	-0.12
For $0.05 < \beta$	-0.18
C_{n_β}:	
For $0 < \beta < 0.1$	0.10
For $0.1 < \beta$	0.16
C_{l_β}	0
$C_{l_{\beta_\alpha}}$:	
For $0 < \alpha < 0.17$	-0.82
For $0.17 < \alpha$	-0.22
C_{l_p}	0.08
C_{l_r}	0.01
$\left(C_{n_r} - C_{n_{\dot{\beta}}}\right)$	-0.06
C_{n_p}	0

TABLE IV

INITIAL CONDITIONS FOR EQUATIONS FOR FIVE DEGREES OF FREEDOM

M	[a]2.25
V, ft/sec	[a]2,100
q_{∞}, lb/sq ft	[a]570
α, radians	0.09
β, radians	0.15
p, radians/sec	16.75
q, radians/sec	2.10
r, radians/sec	0.01
$\dot{p}$, radians/sec^2	-282
$\dot{q}$, radians/sec^2	-38.2
$\dot{r}$, radians/sec^2	-17.2

[a]Average values from 39 seconds to 45 seconds on flight record.

L1186

TABLE V

INITIAL CONDITIONS FOR SIMPLIFIED EQUATIONS

M	[a]2.25
V, ft/sec	[a]2,100
q_{∞}, lb/sq ft	[a]570
α, radians	0.09
β, radians	0.15
p, radians/sec	12.2
$\dot{p}$, radians/sec^2	-242

[a]Average values from 39 seconds to 45 seconds on flight record.

L-1186

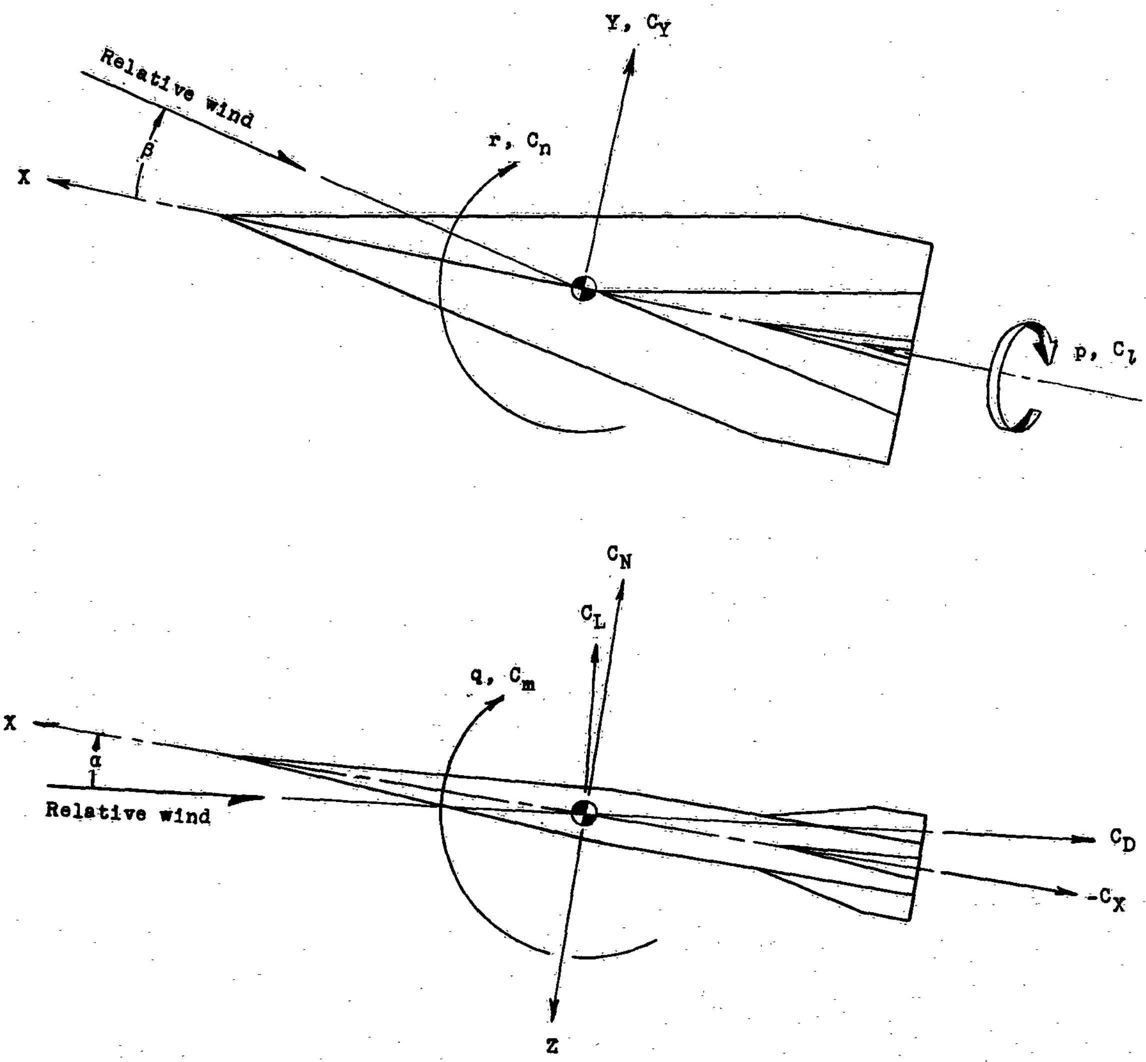

Figure 1.- Body-axis system. Arrows indicate positive directions.

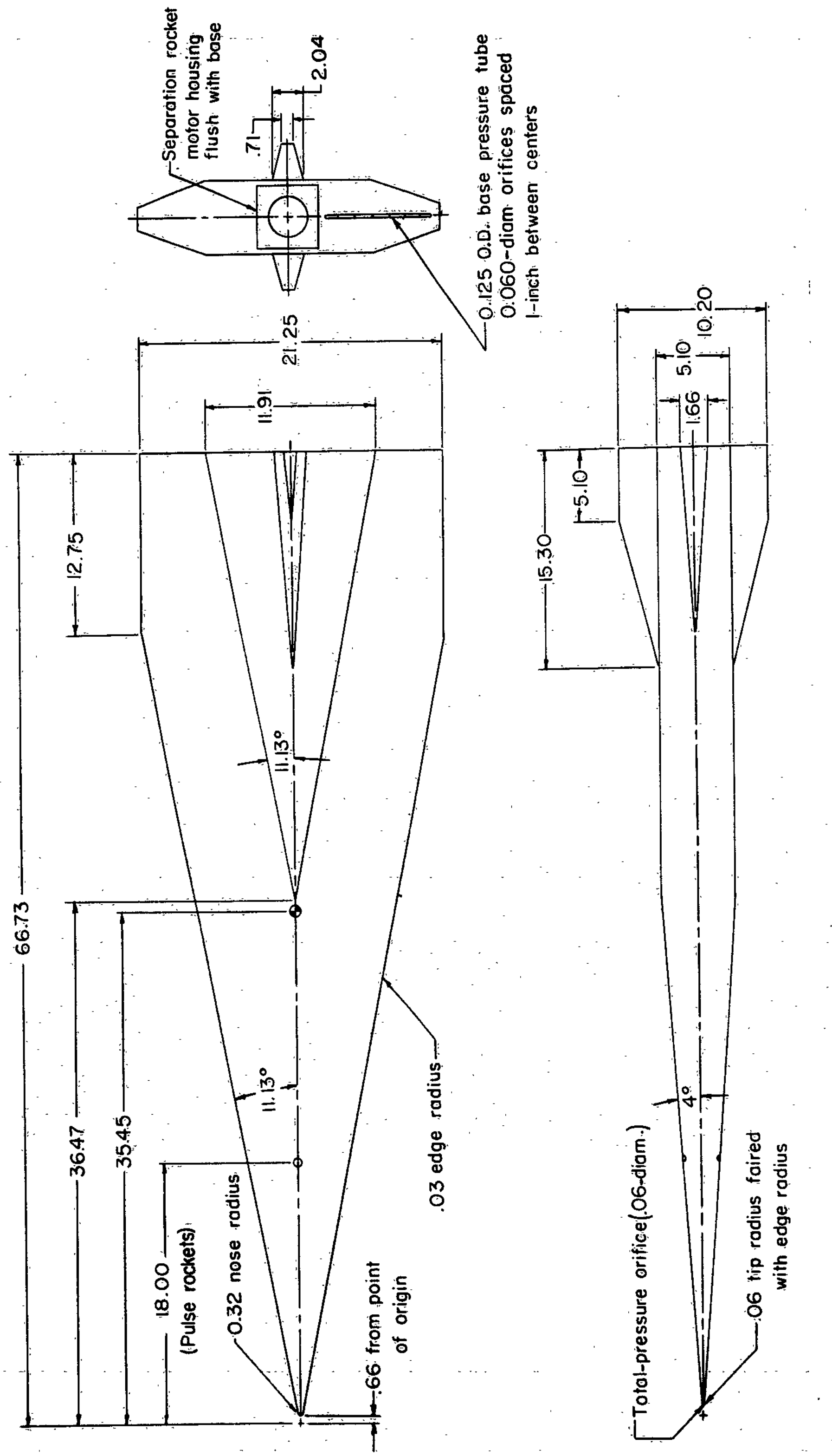

(a) Rocket-propelled model.

Figure 2.- Details and dimensions of models. (All dimensions are in inches.)

L-1186

L-1186

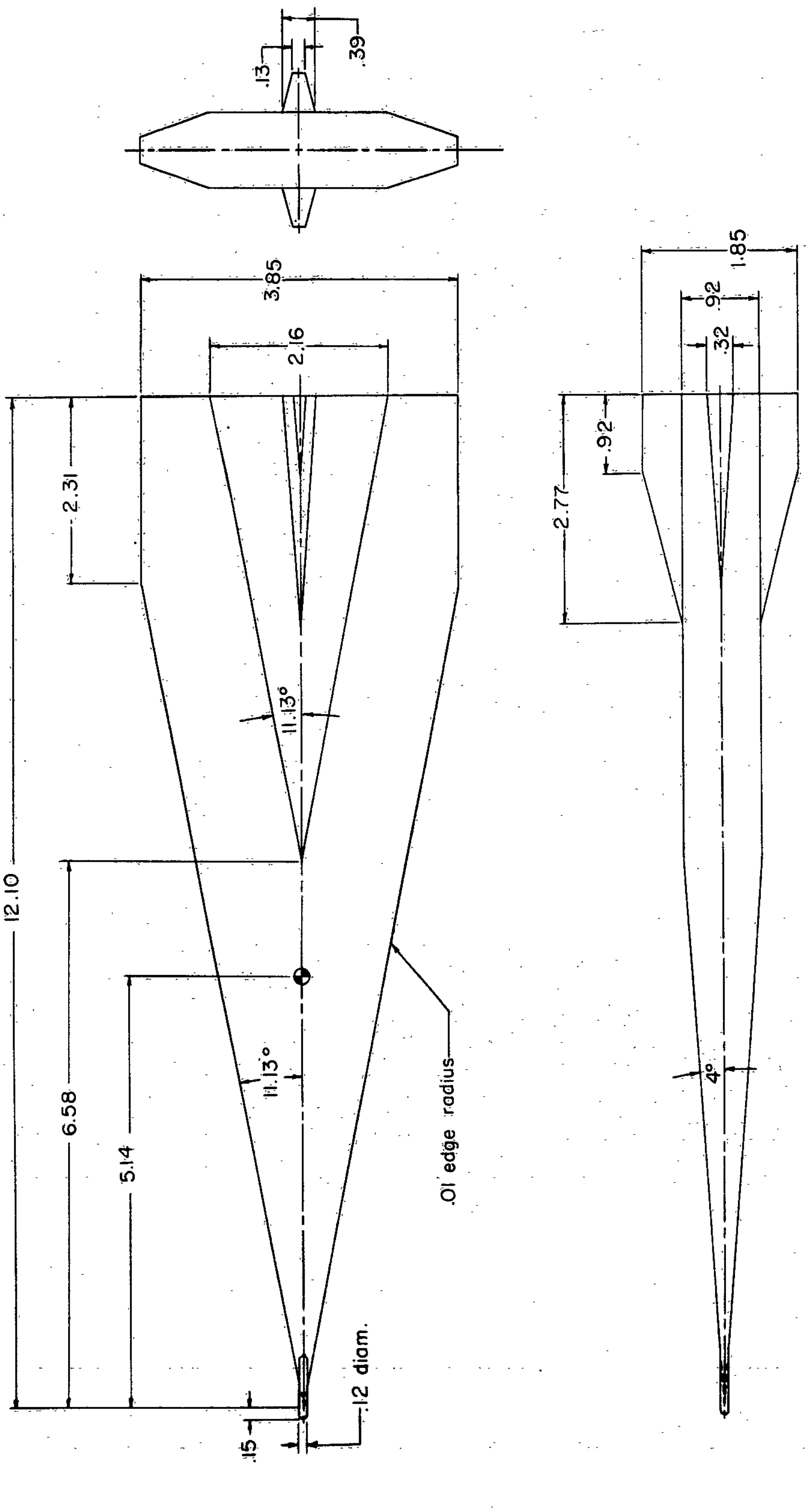

(b) Helium-gun model.

Figure 2.- Concluded.

(a) Planform view of rocket model.

Figure 3.- Photographs of models. L-58-1065a

L-1186

L-58-1064a

(b) Three-quarter rear view of rocket model.

Figure 3.- Concluded.

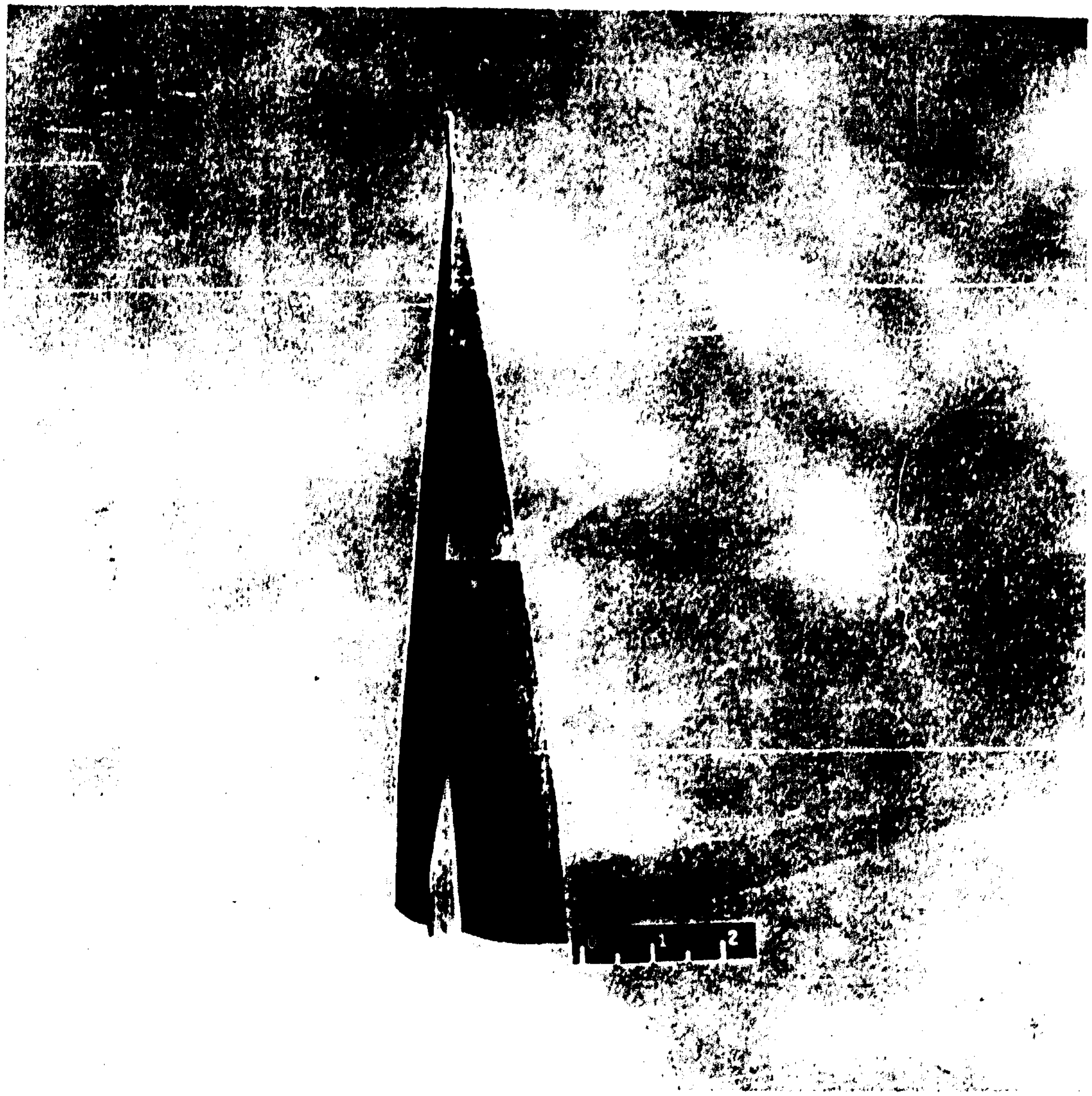

Figure 4.- Helium-gun model. L-59-489.1

L-1186

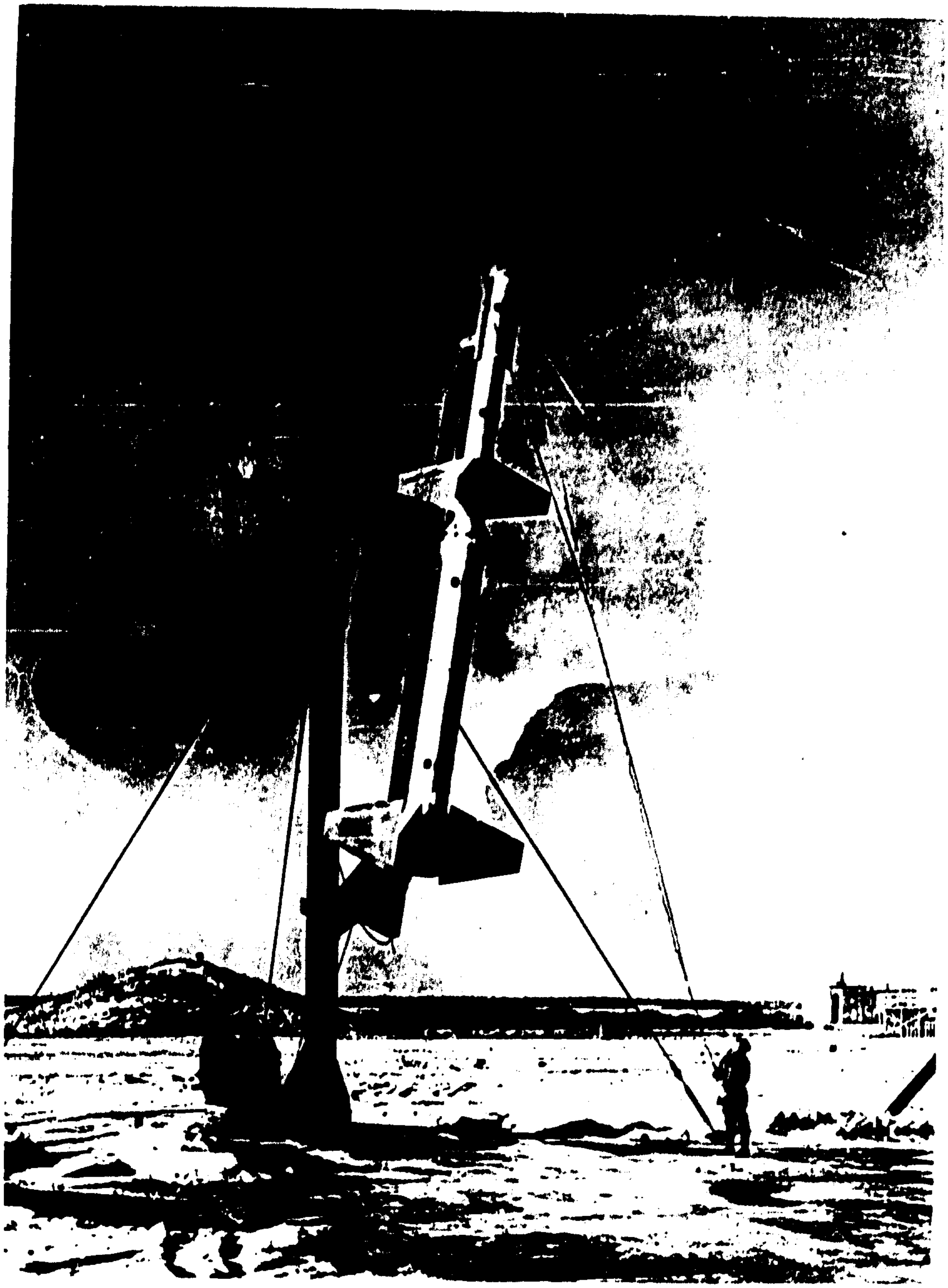

L-58-1361a

Figure 5.- Rocket model and boosters on launcher.

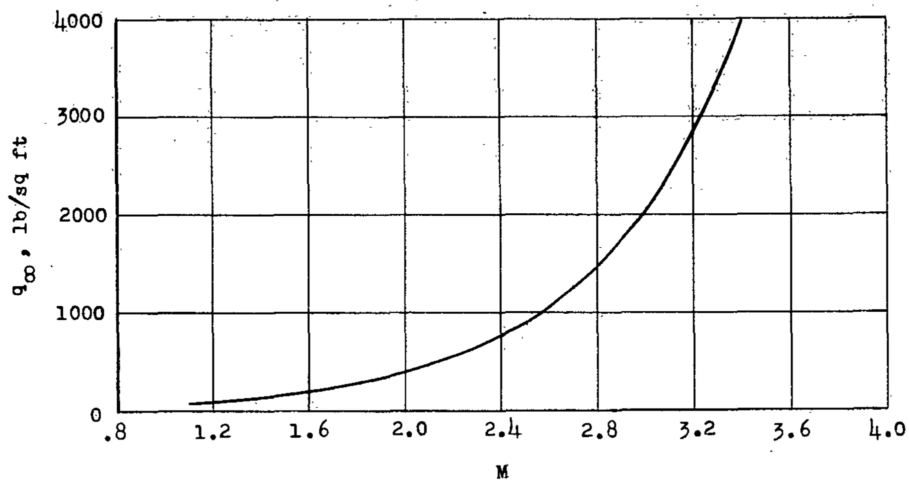

(a) Free-stream dynamic pressure.

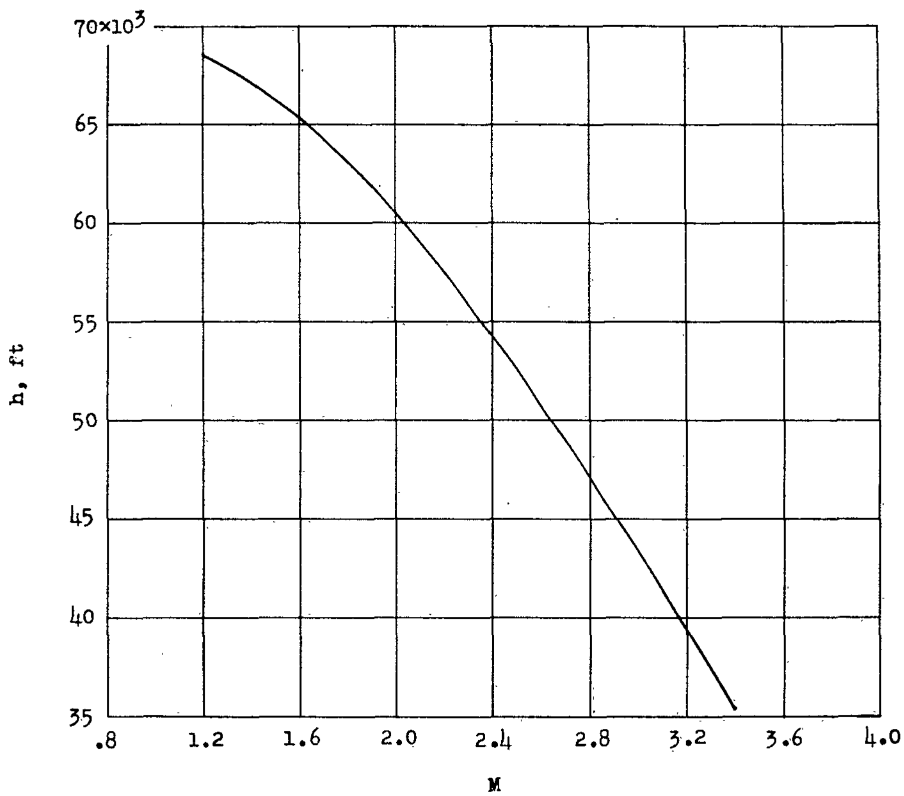

(b) Altitude.

Figure 6.- Variations of free-stream dynamic pressure and altitude with Mach number for the rocket model.

L-1186

L-1186

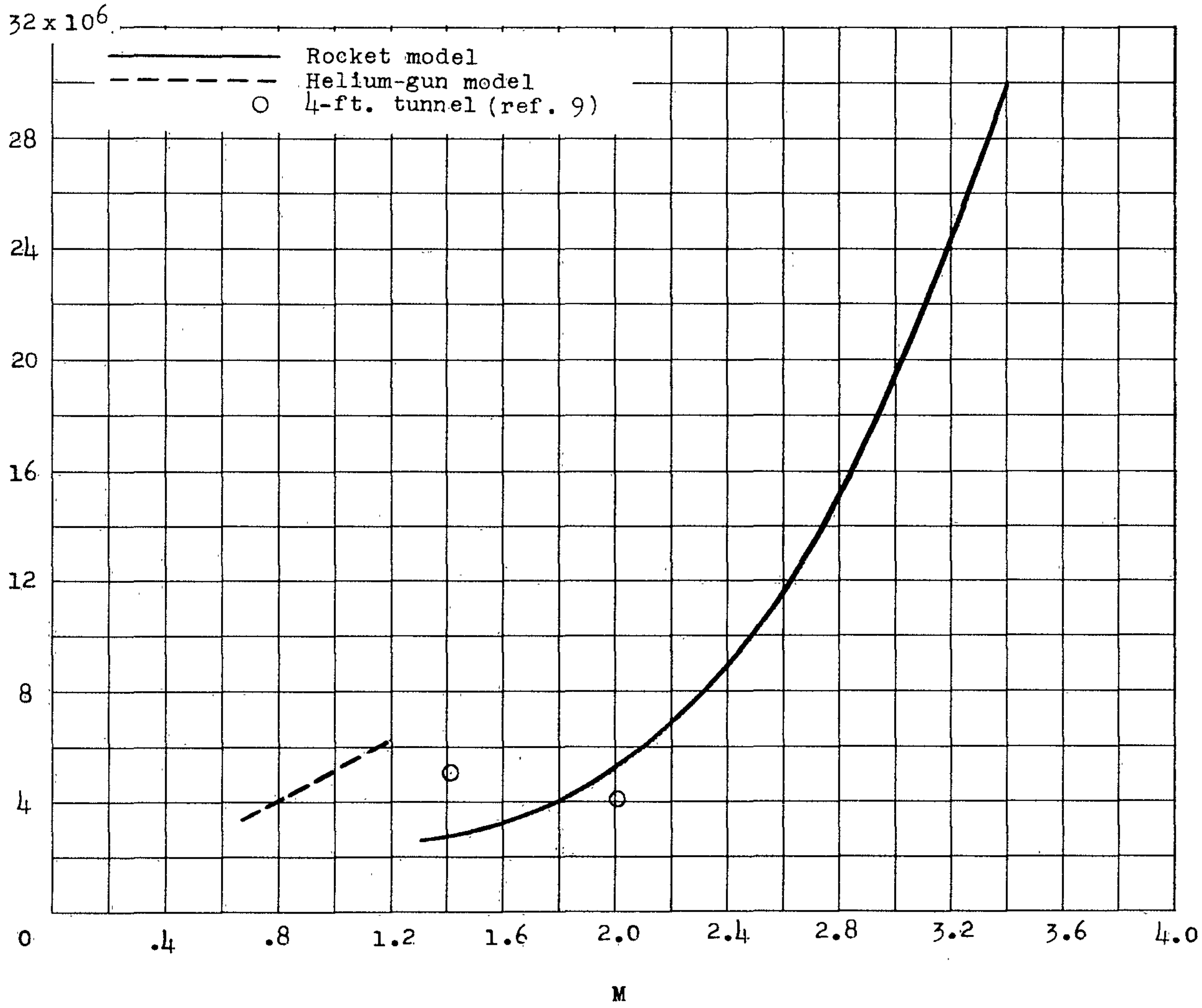

Figure 7.- Variations of Reynolds number with Mach number for flight models and for wind-tunnel tests of reference 9. Reynolds number is based on mean aerodynamic chord.

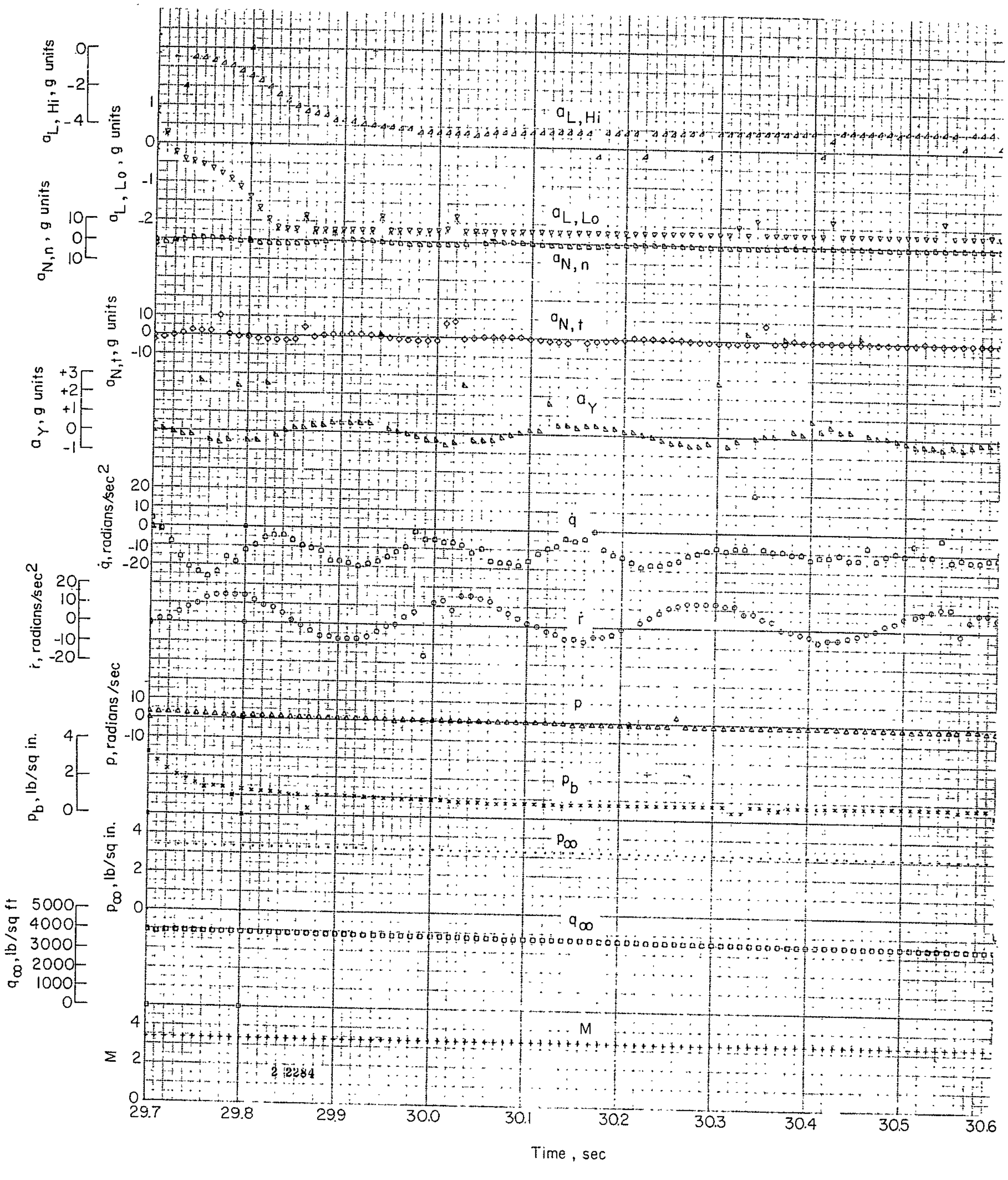

(a) Time interval after model separated from booster.

Figure 8.- Variations of basic data and free-stream conditions with time for three typical time intervals of the flight.

L-1186

L-1186

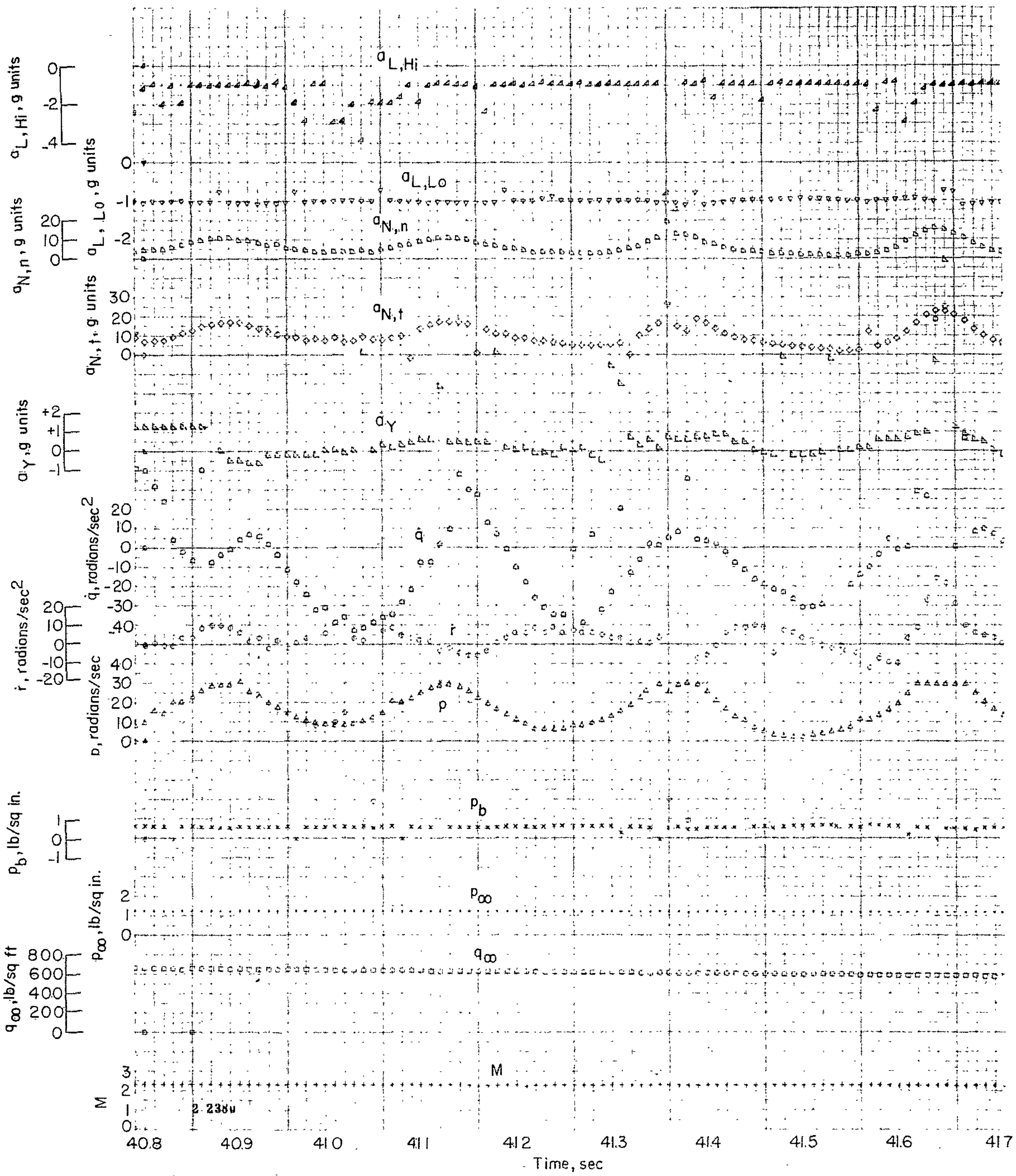

(b) Time interval after first pulse rocket fired, 40.8 to 41.7 sec.

Figure 8.- Continued.

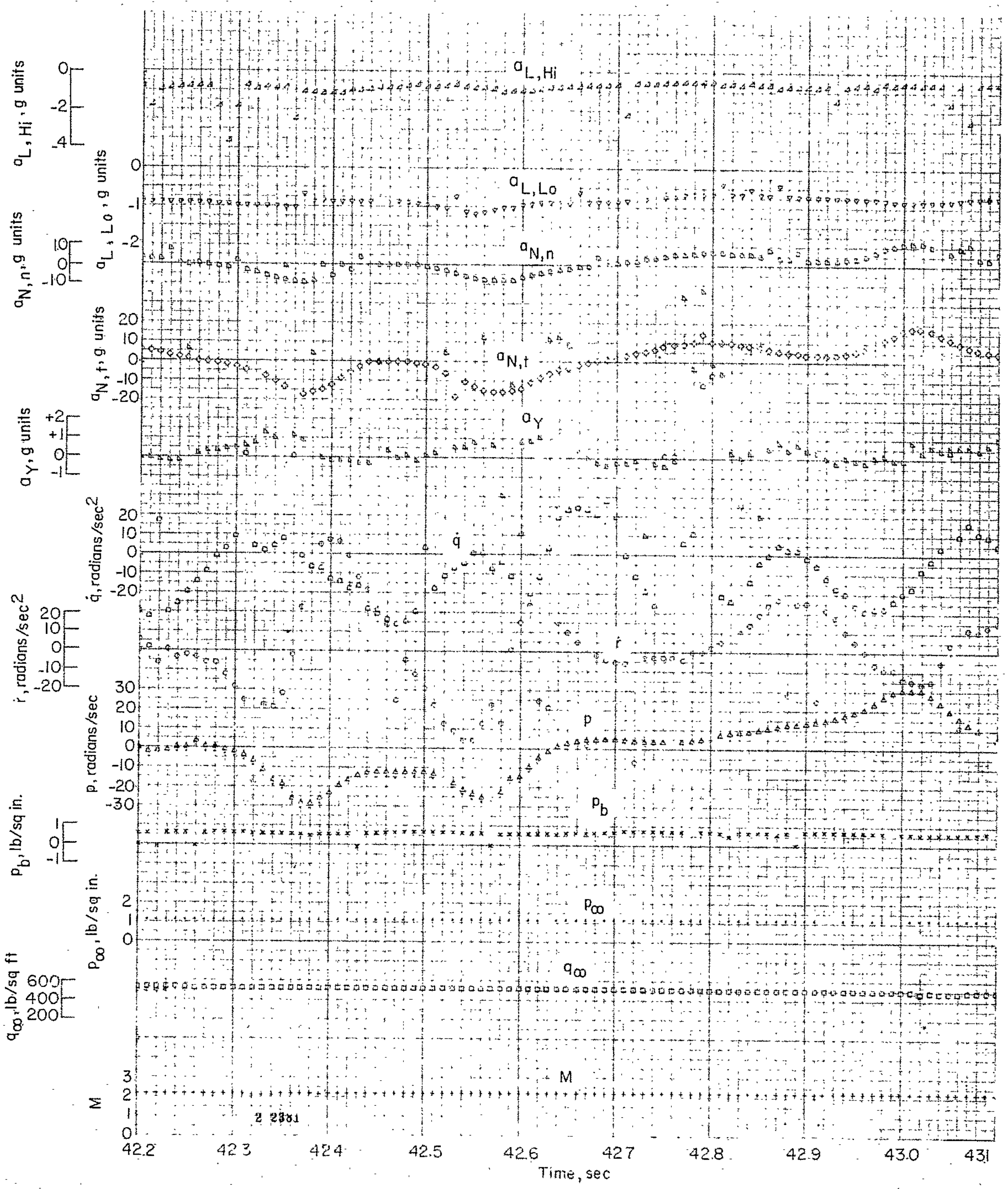

(c) Time interval after first pulse rocket fired, 42.2 to 43.1 sec.

Figure 8.- Concluded.

L-1100

L-1186

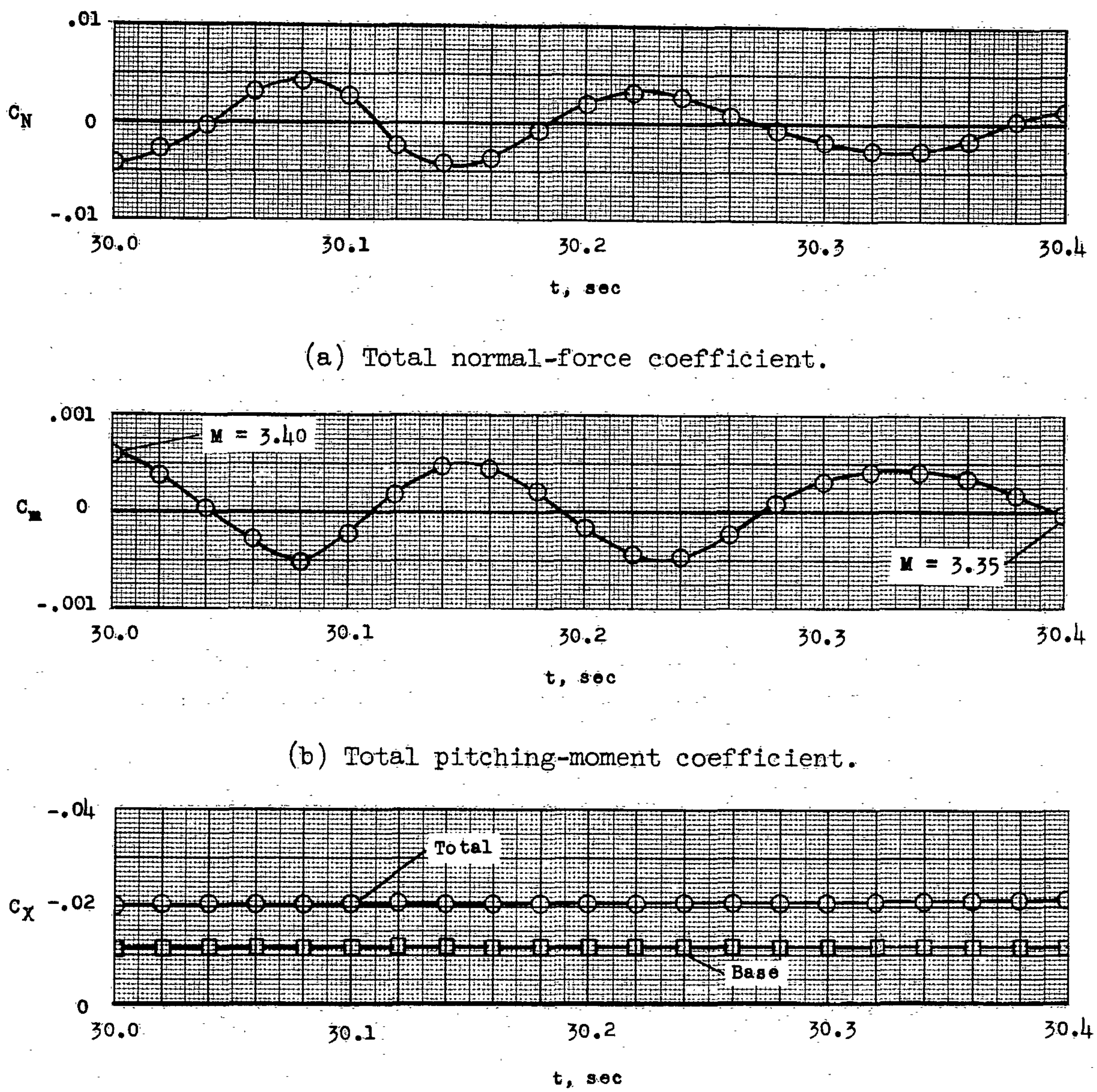

(a) Total normal-force coefficient.

(b) Total pitching-moment coefficient.

(c) Total axial-force and base axial-force coefficients.

Figure 9.- Time histories of C_N, C_m, and C_X. $M \approx 3.4$.

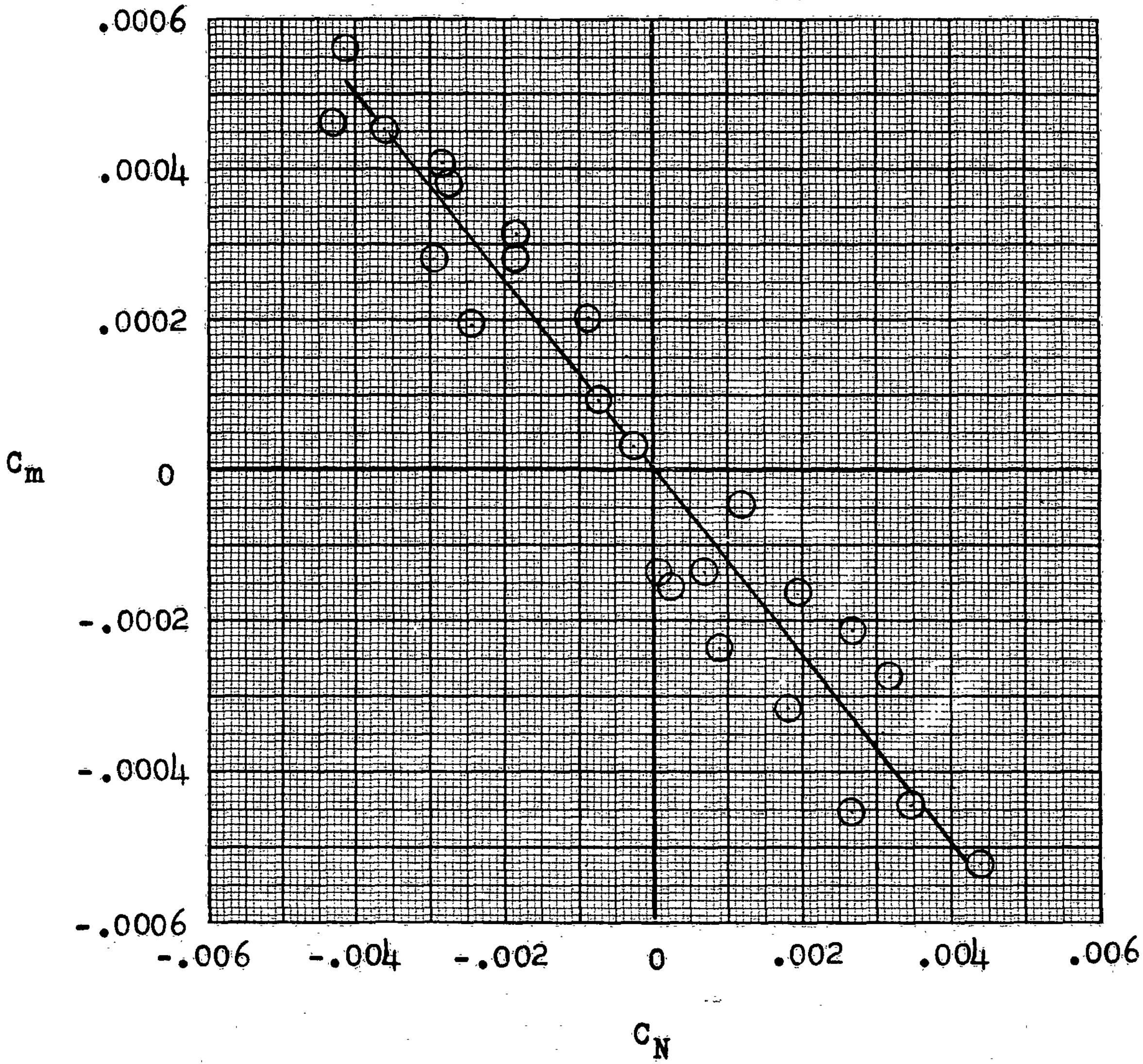

Figure 10.- Variation of C_m with C_N. $M \approx 3.4$.

L-1186

L-1186

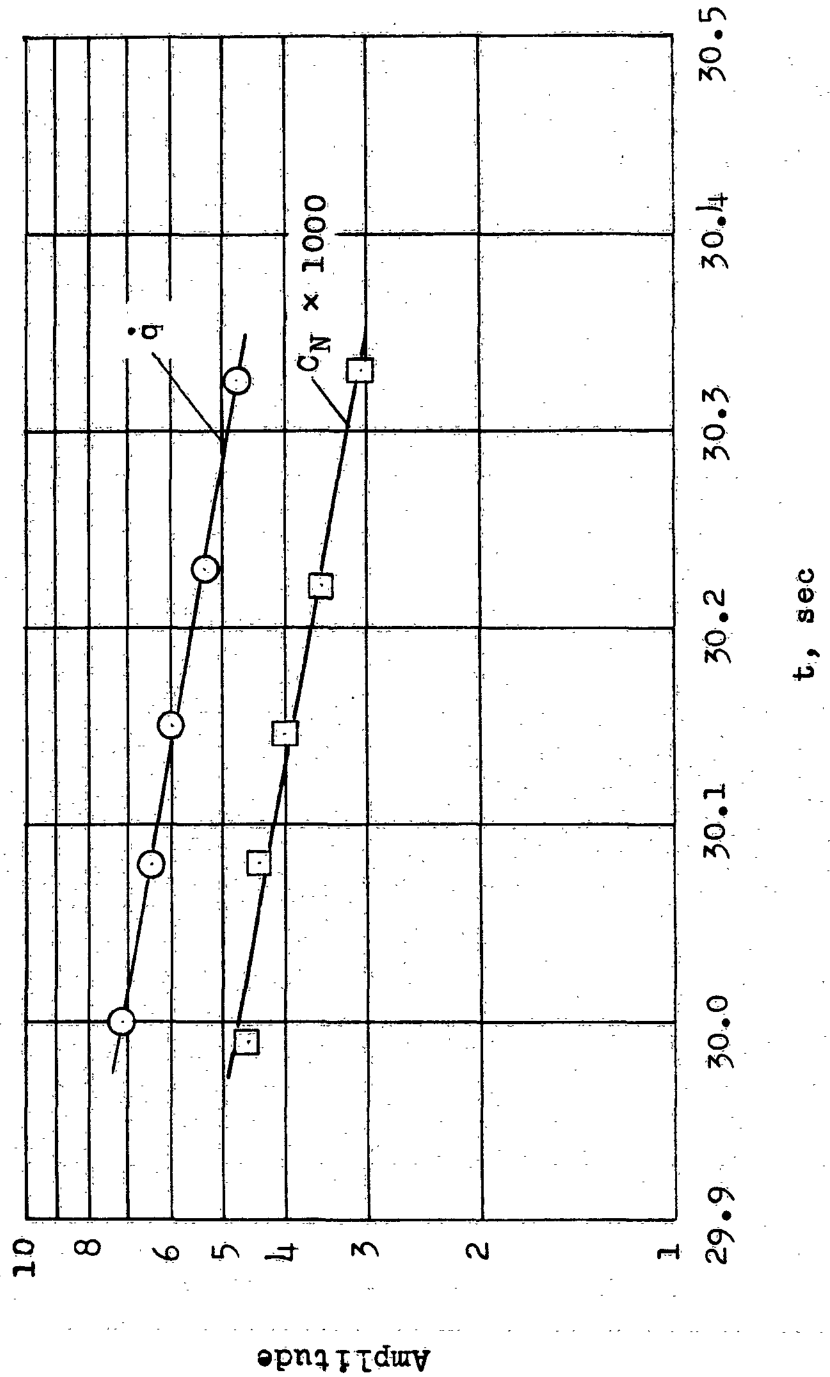

Figure 11.- Amplitudes of $\dot{q}$ and C_N as a function of time. $M \approx 3.4$.

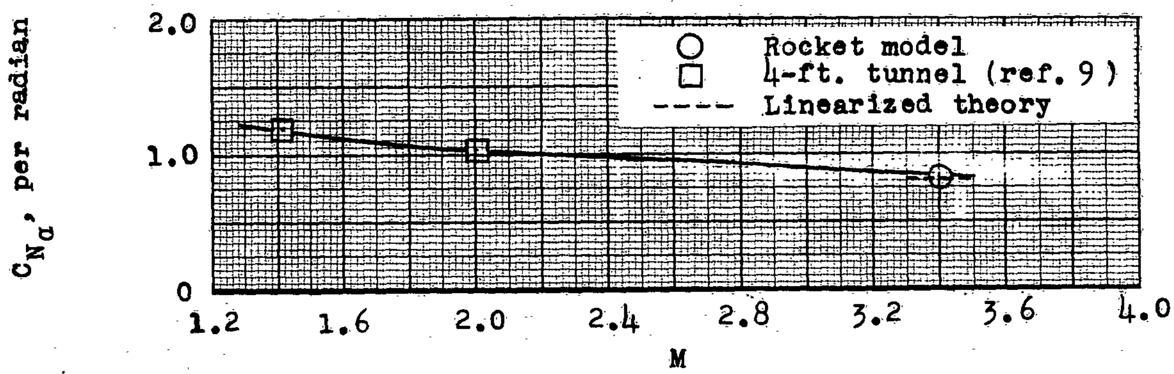

(a) Slope of normal-force coefficient.

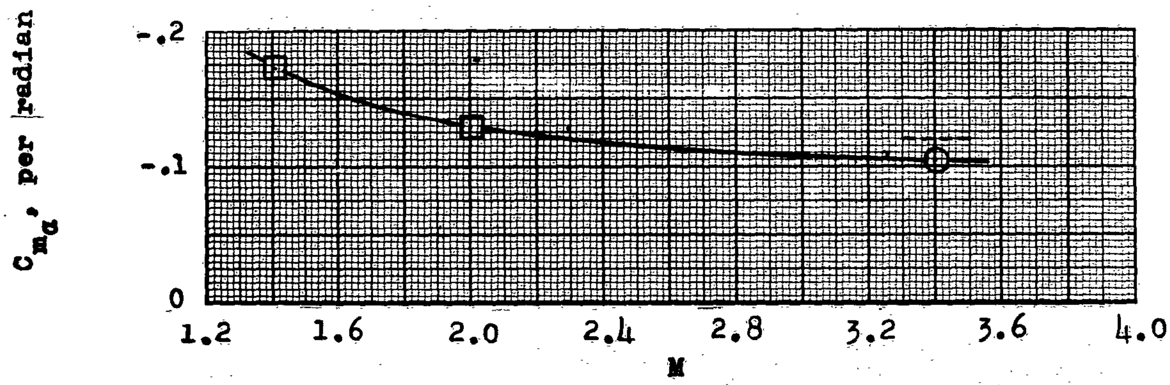

(b) Slope of pitching-moment coefficient.

Figure 12.- Variations of the static stability derivatives in pitch with Mach number at zero angle of attack as determined from wind-tunnel tests, flight test, and linearized theory.

L-1186

L-1186

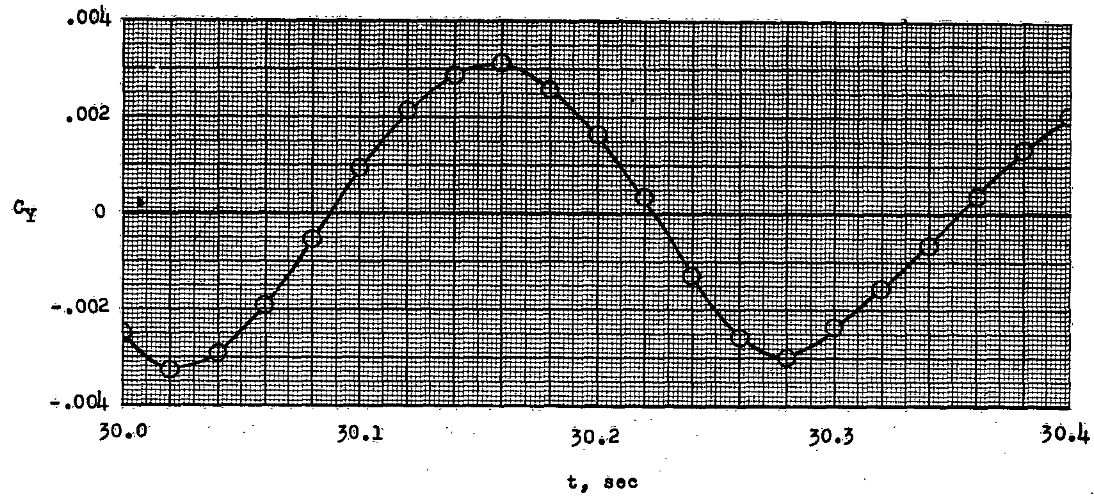

(a) Total side-force coefficient.

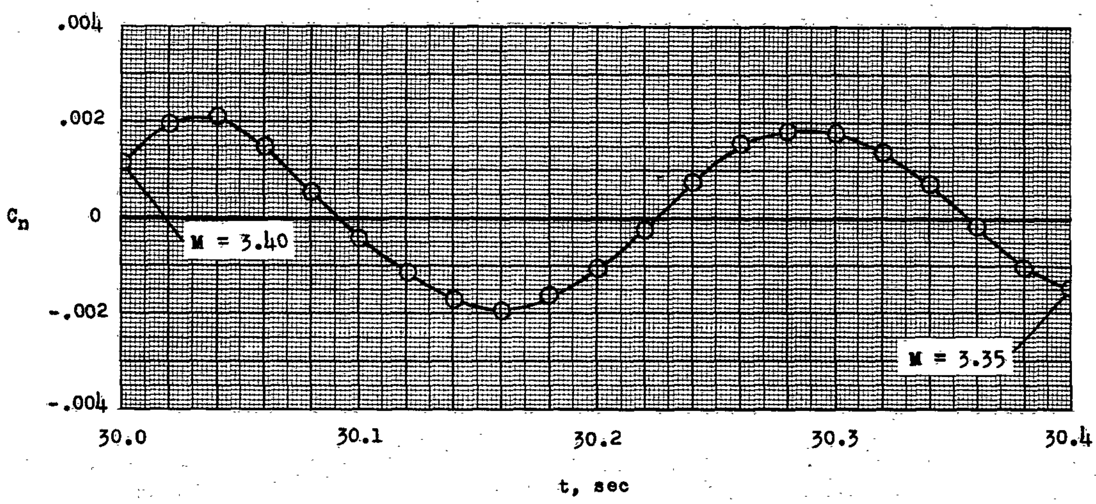

(b) Total yawing-moment coefficient.

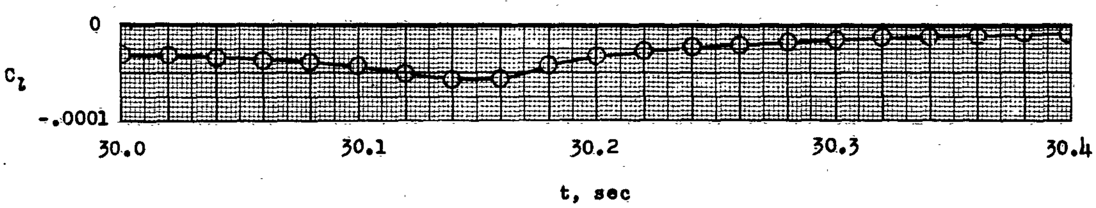

(c) Total rolling-moment coefficient.

Figure 13.- Time histories of C_Y, C_n, and C_l. $M \approx 3.4$.

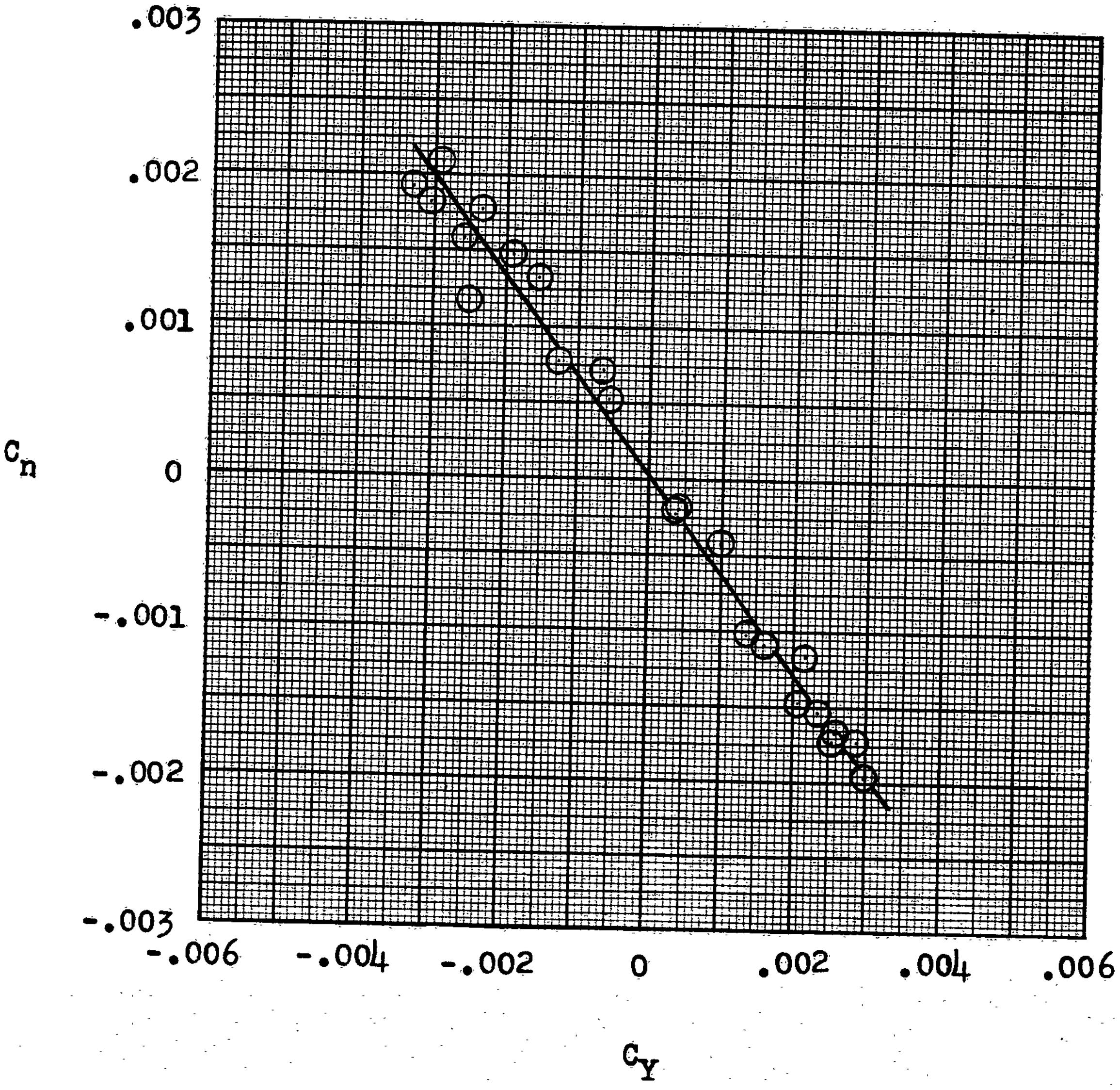

Figure 14.- Variation of C_n with C_Y. $M \approx 3.4$.

L-1186

L-1186

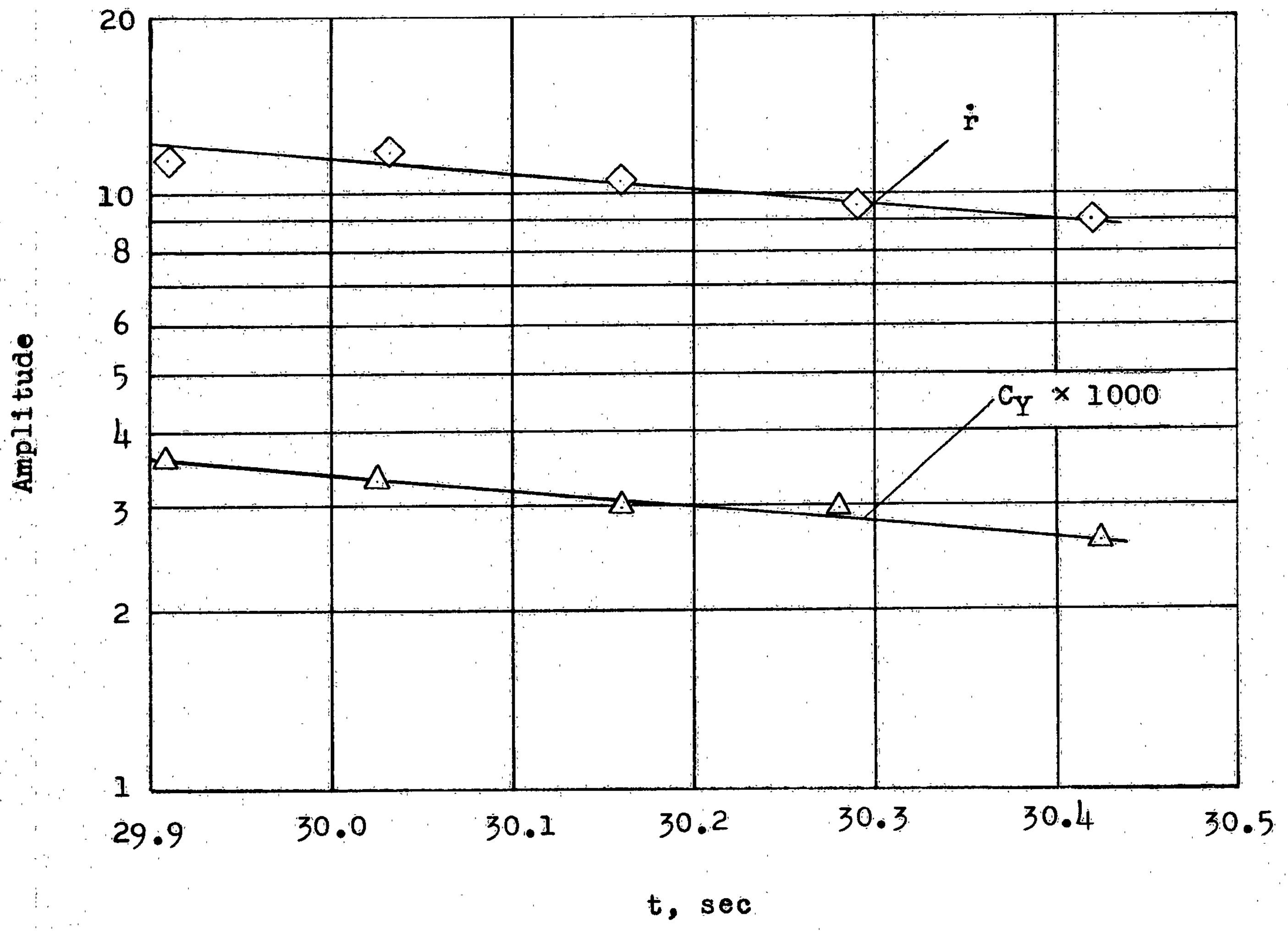

Figure 15.- Amplitudes of $\dot{r}$ and C_Y as a function of time. $M \approx 3.4$.

L-1186

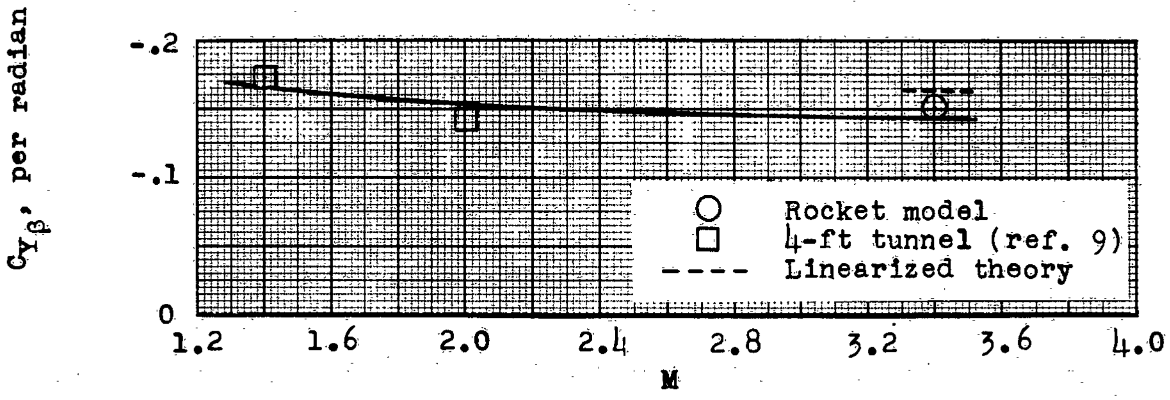

(a) Slope of side-force coefficient.

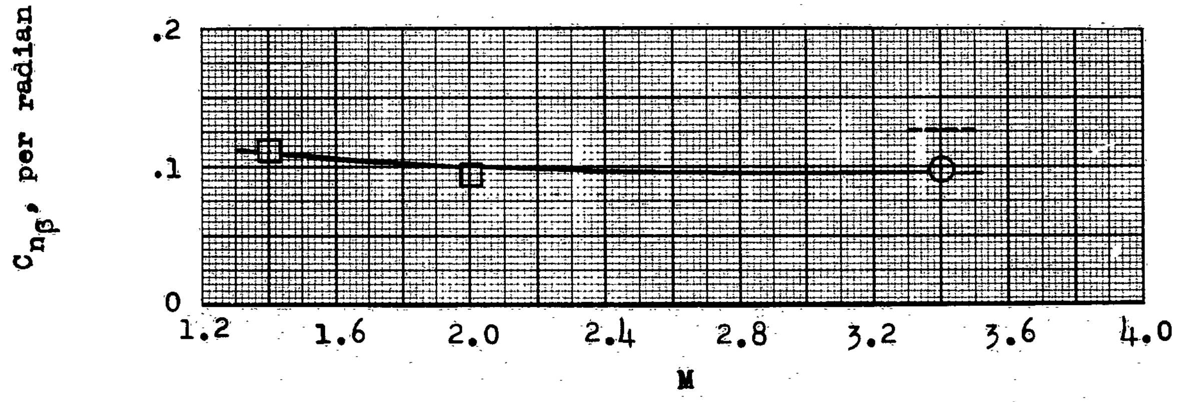

(b) Slope of yawing-moment coefficient.

Figure 16.- Variations of the static stability derivatives in yaw with Mach number at zero angle of sideslip as determined from wind-tunnel tests, flight test, and linearized theory.

L-1186

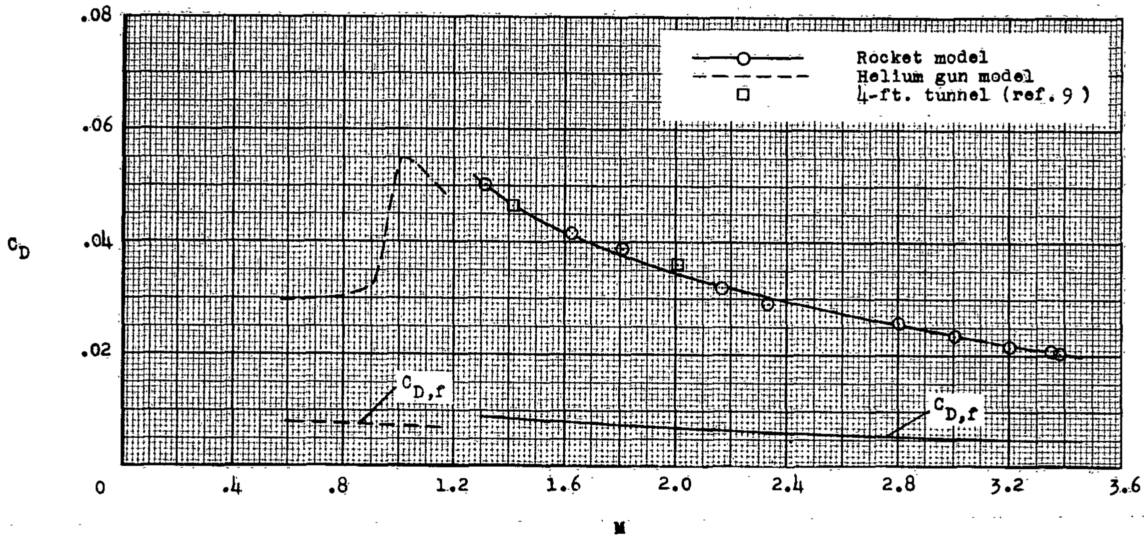

(a) Total-drag and computed friction-drag coefficients.

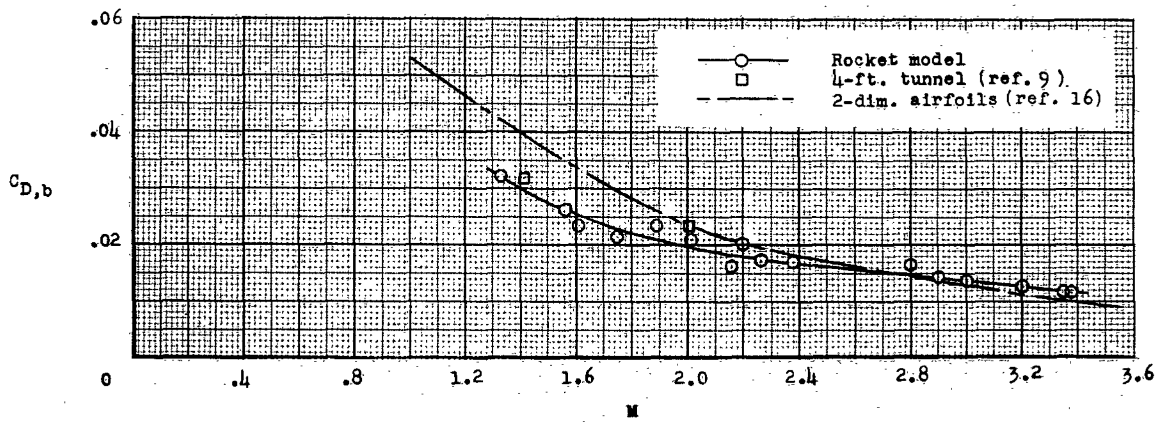

(b) Base-drag coefficients.

Figure 17.- Variations of total-drag, friction-drag, and base-drag coefficients with Mach number at approximately zero angle of attack.

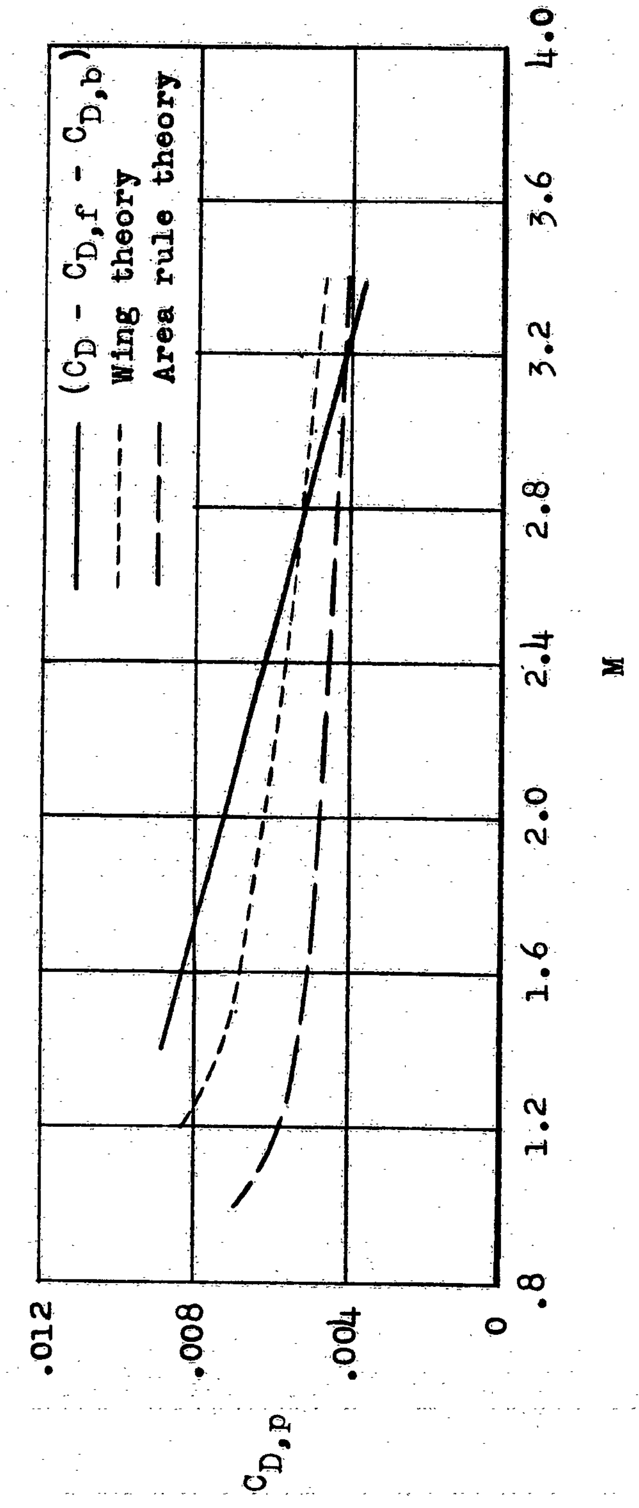

Figure 18.- Comparison of experimental and theoretical pressure drags at zero angle of attack.

L-1186

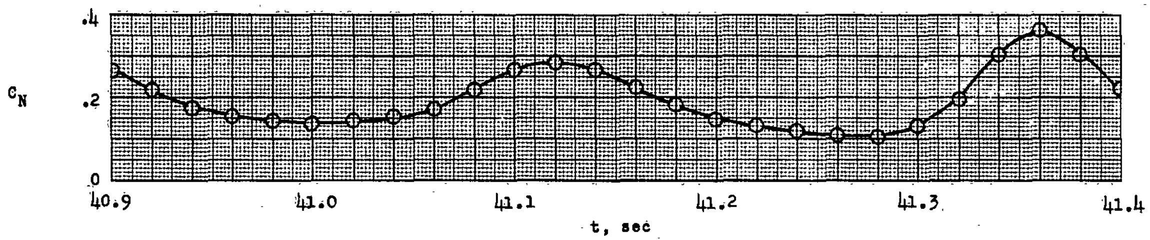

(a) Total normal-force coefficient.

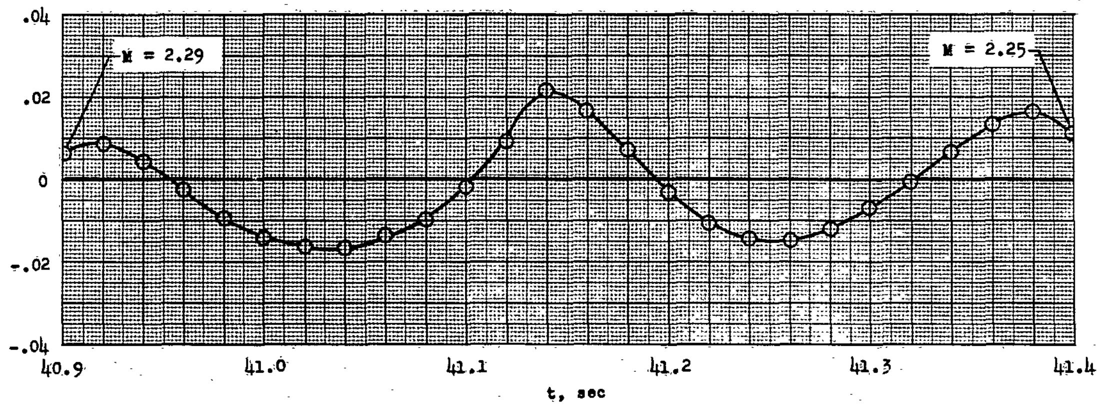

(b) Total pitching-moment coefficient.

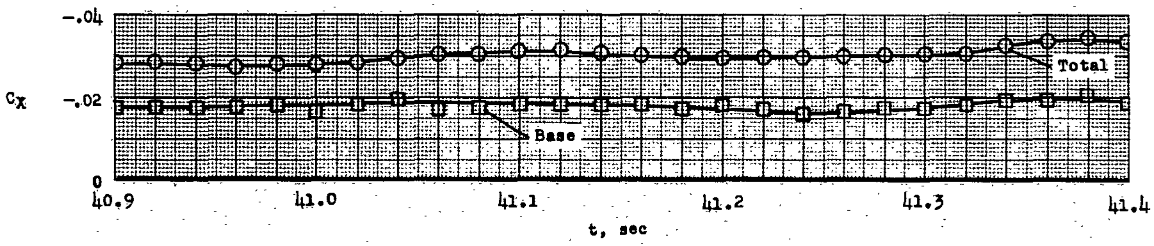

(c) Total axial-force and base axial-force coefficients.

Figure 19.- Variations of total-force and total-moment coefficients with time. $M \approx 2.3$.

L-1186

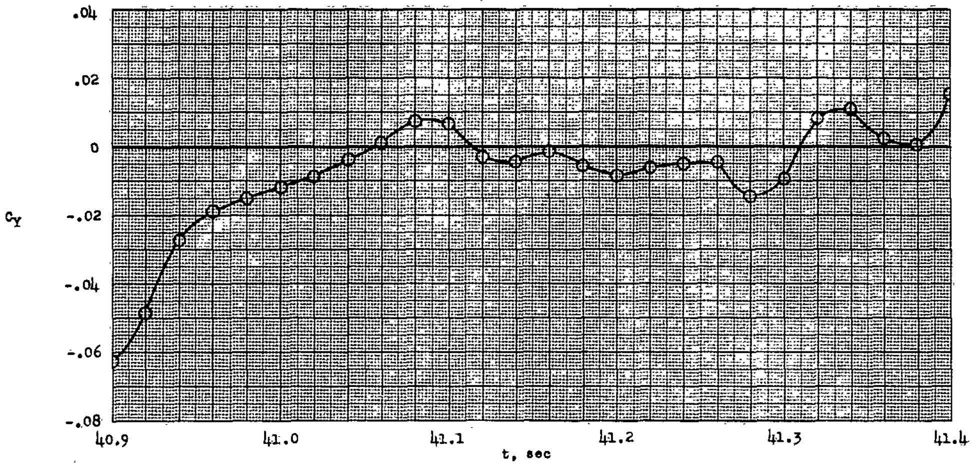

(d) Total side-force coefficient.

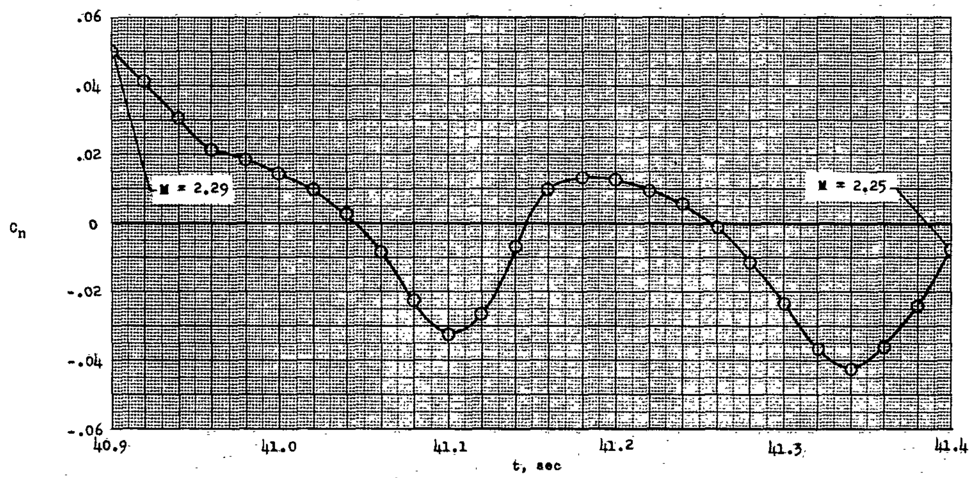

(e) Total yawing-moment coefficient.

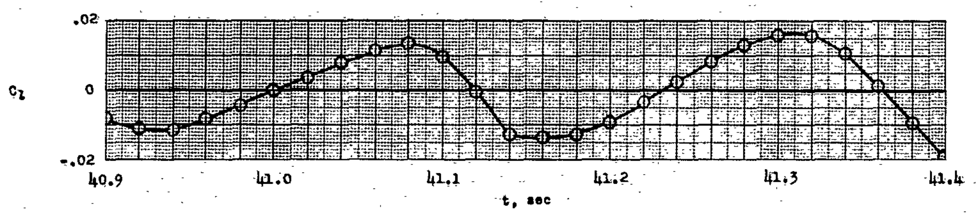

(f) Total rolling-moment coefficient.

Figure 19.- Continued.

L-1186

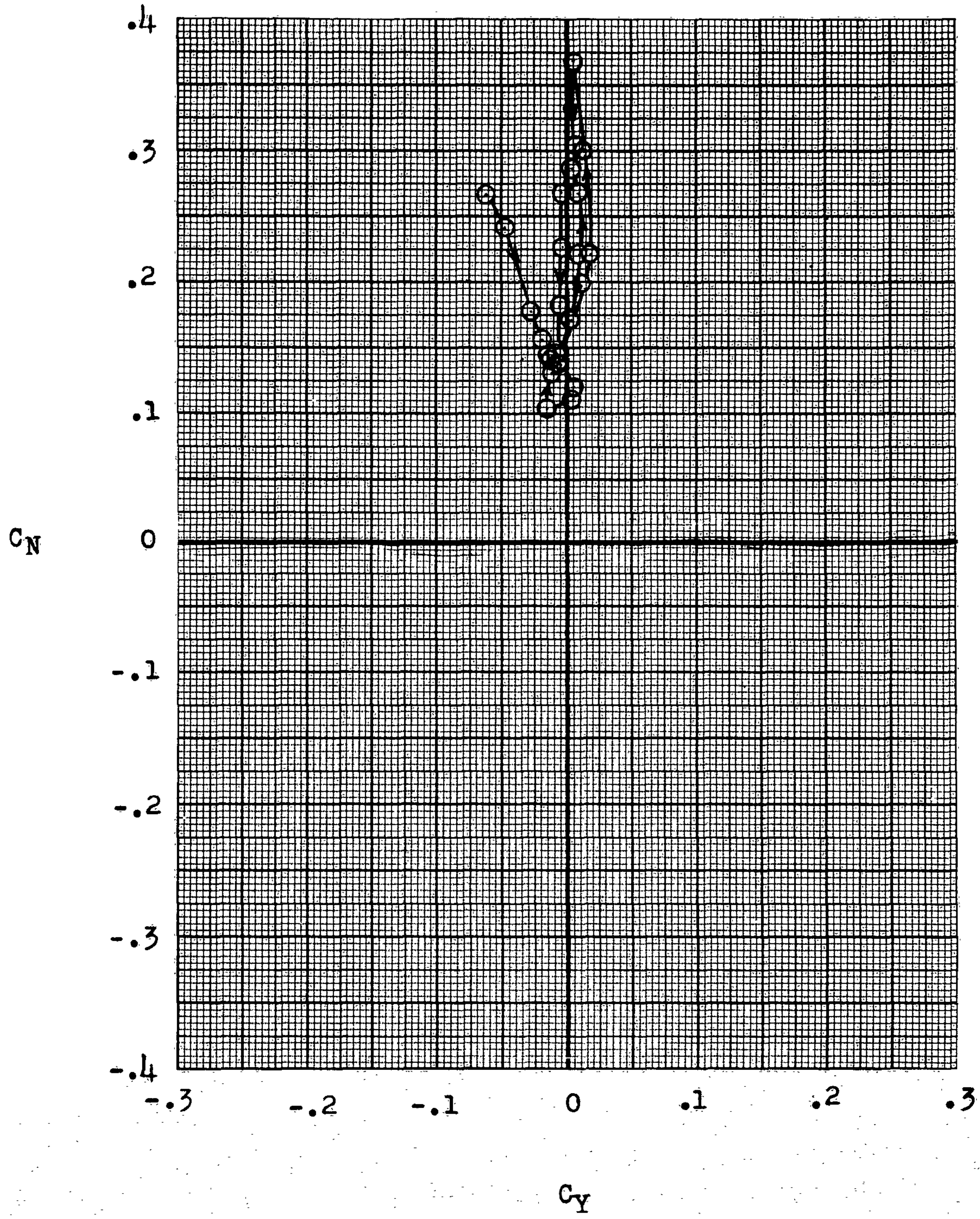

(g) Variation of normal-force coefficient with side-force coefficient.

Figure 19.- Concluded.

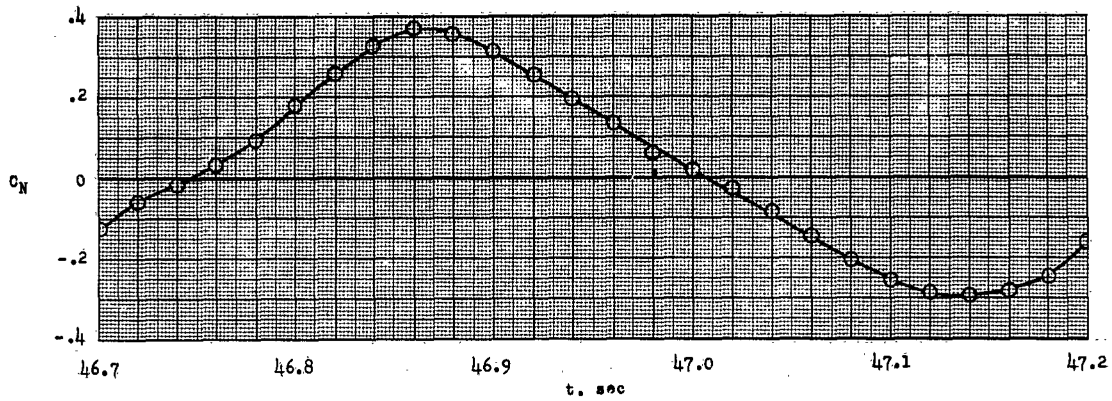

(a) Total normal-force coefficient.

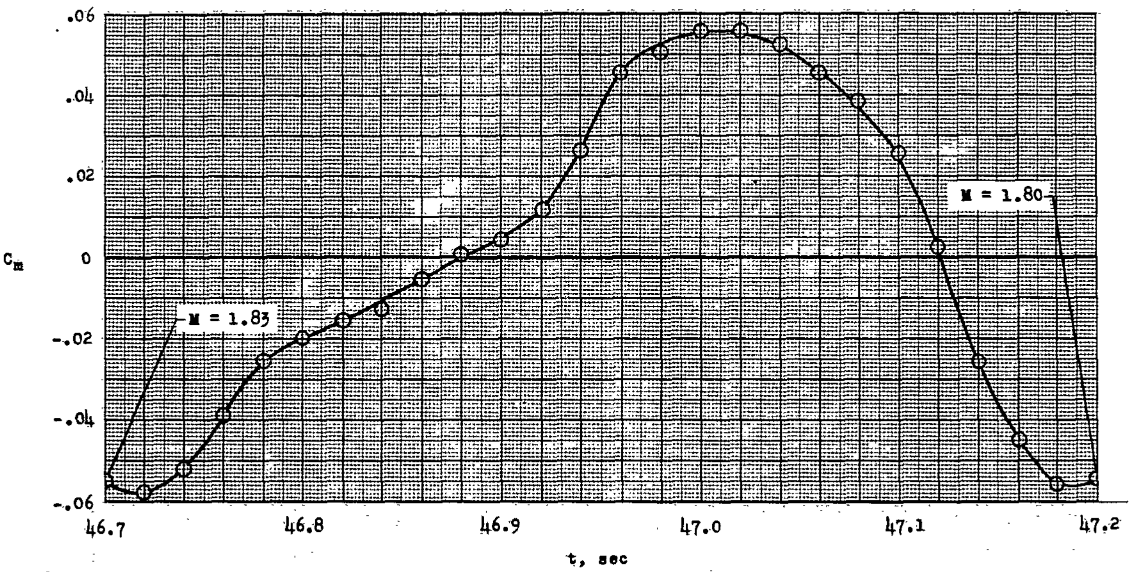

(b) Total pitching-moment coefficient.

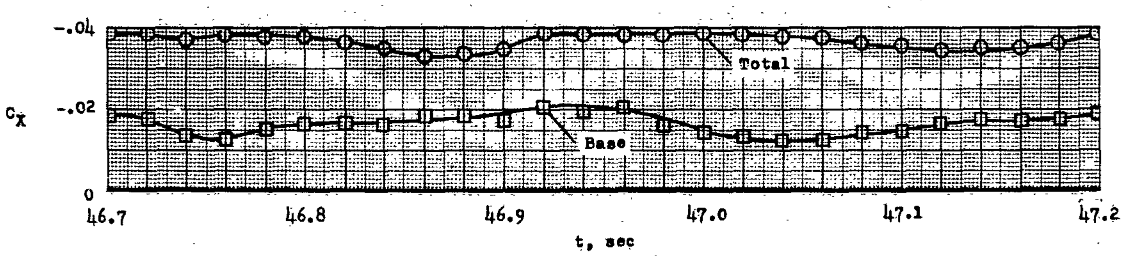

(c) Total axial-force and base axial-force coefficients.

Figure 20.- Variations of total-force and total-moment coefficients with time. $M \approx 1.8$.

L-1186

L-1186

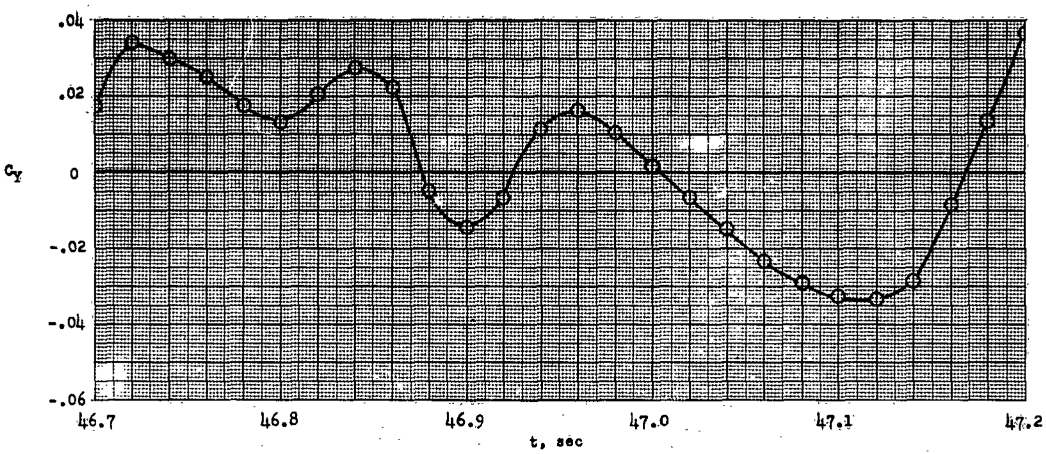

(d) Total side-force coefficient.

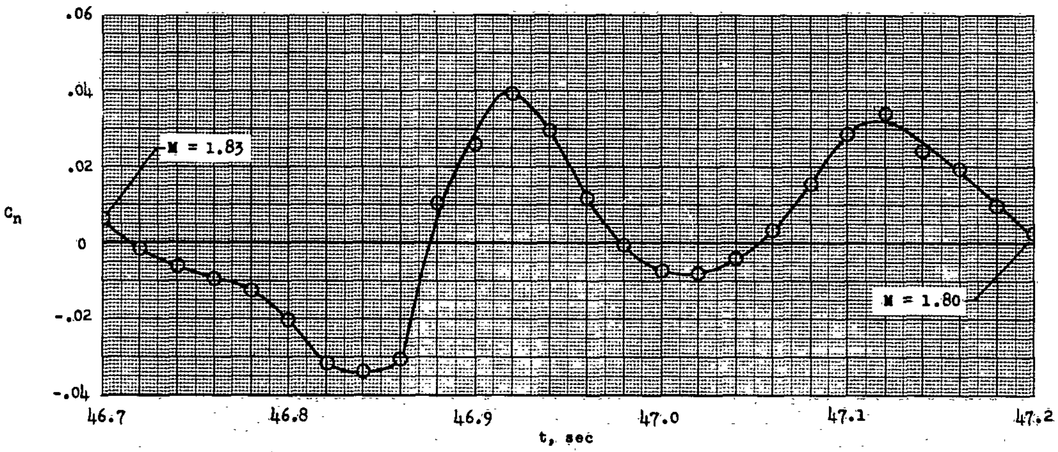

(e) Total yawing-moment coefficient.

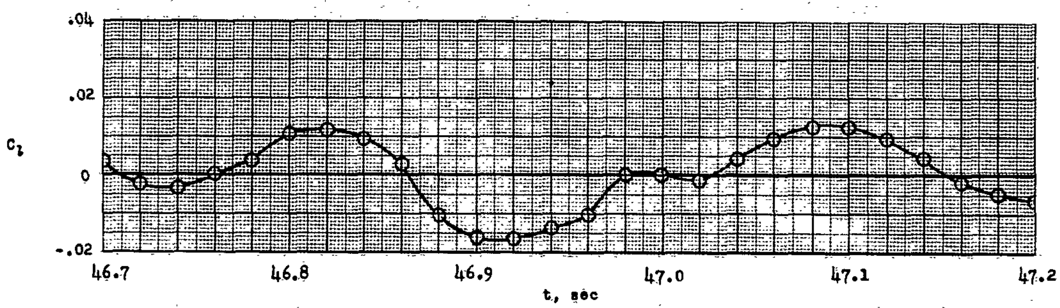

(f) Total rolling-moment coefficient.

Figure 20.- Continued.

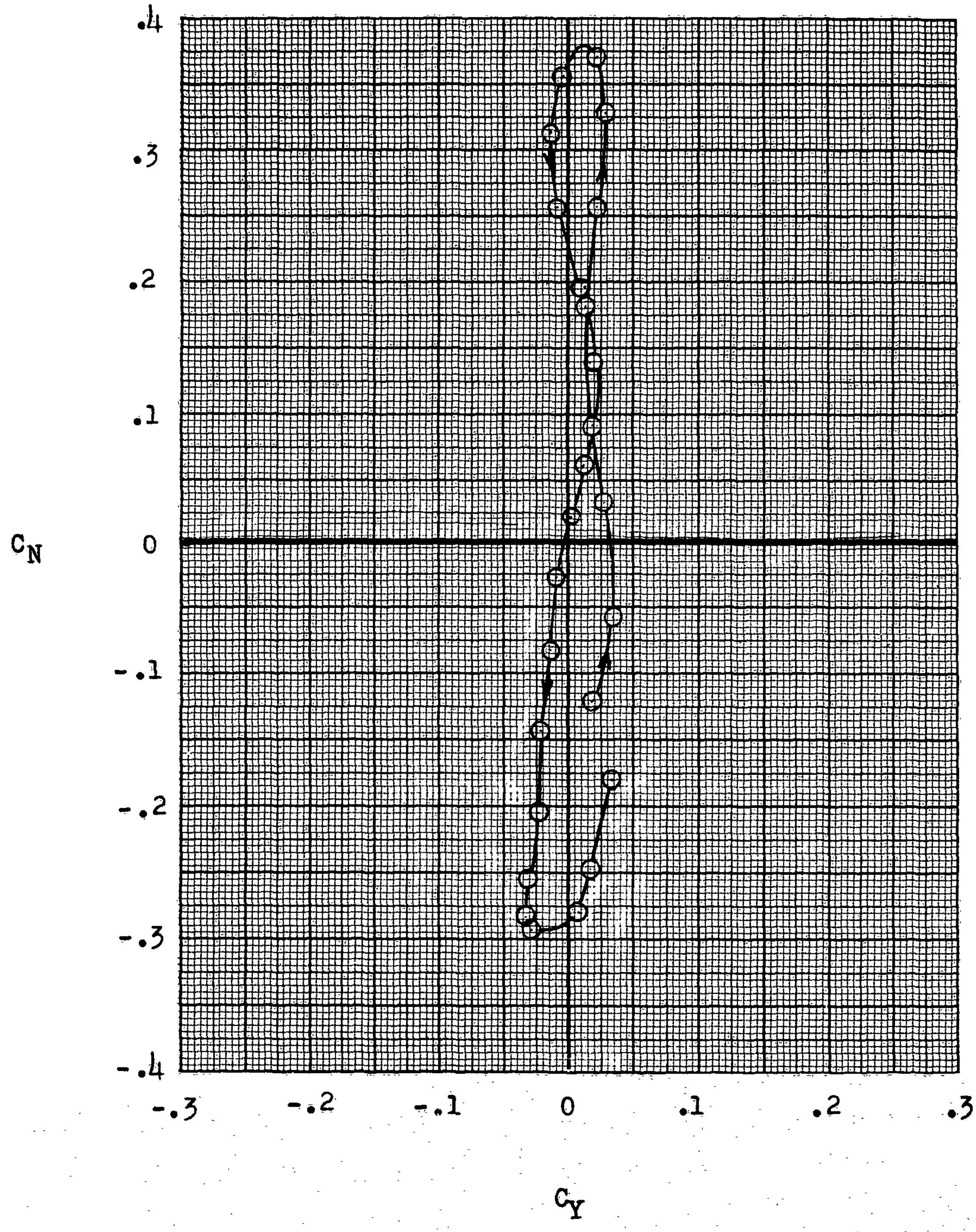

(g) Variation of normal-force coefficient with side-force coefficient.

Figure 20.- Concluded.

L-1186

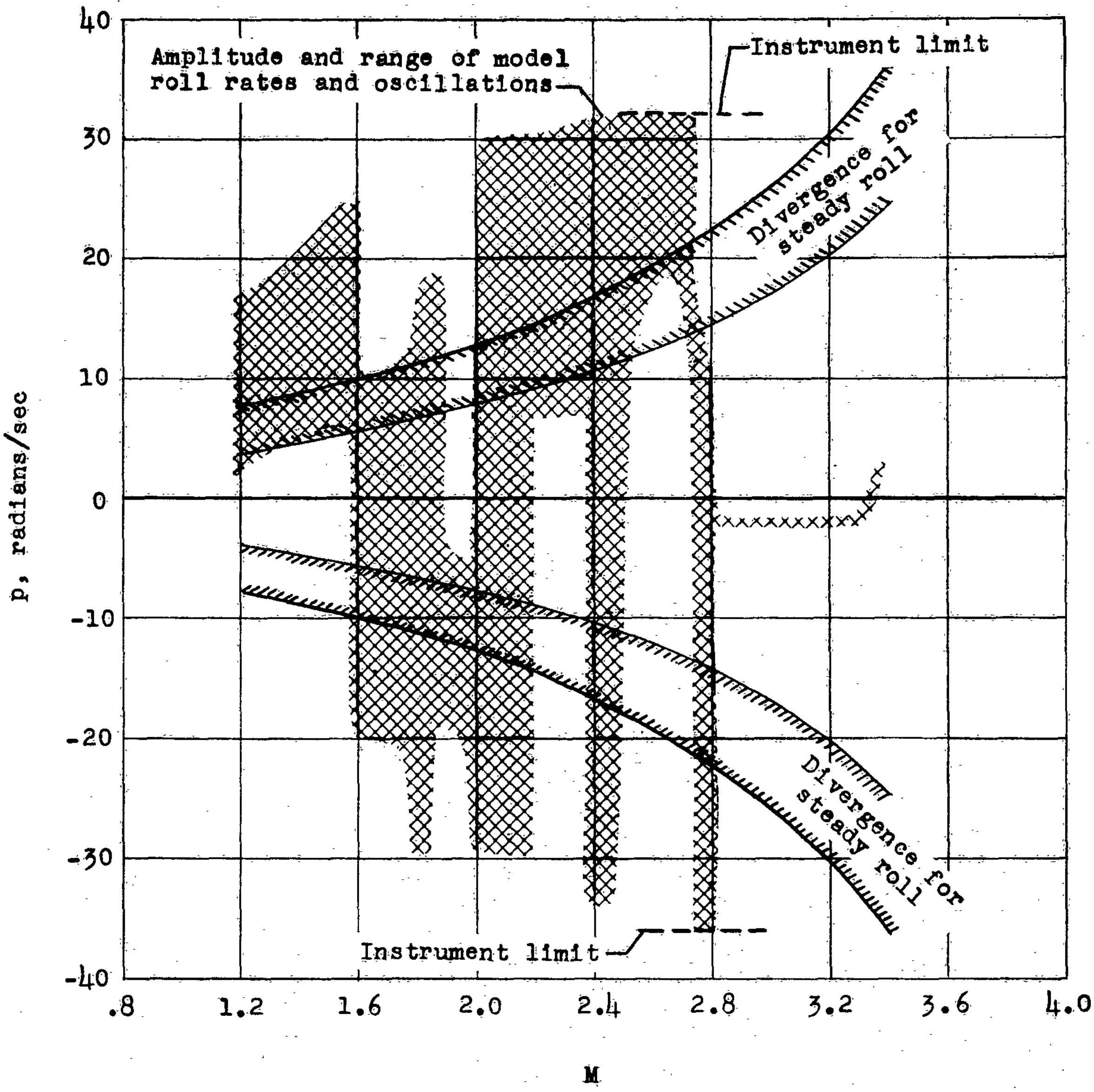

Figure 21.- Variations of the amplitudes and ranges of roll rates with Mach number for the rocket model.

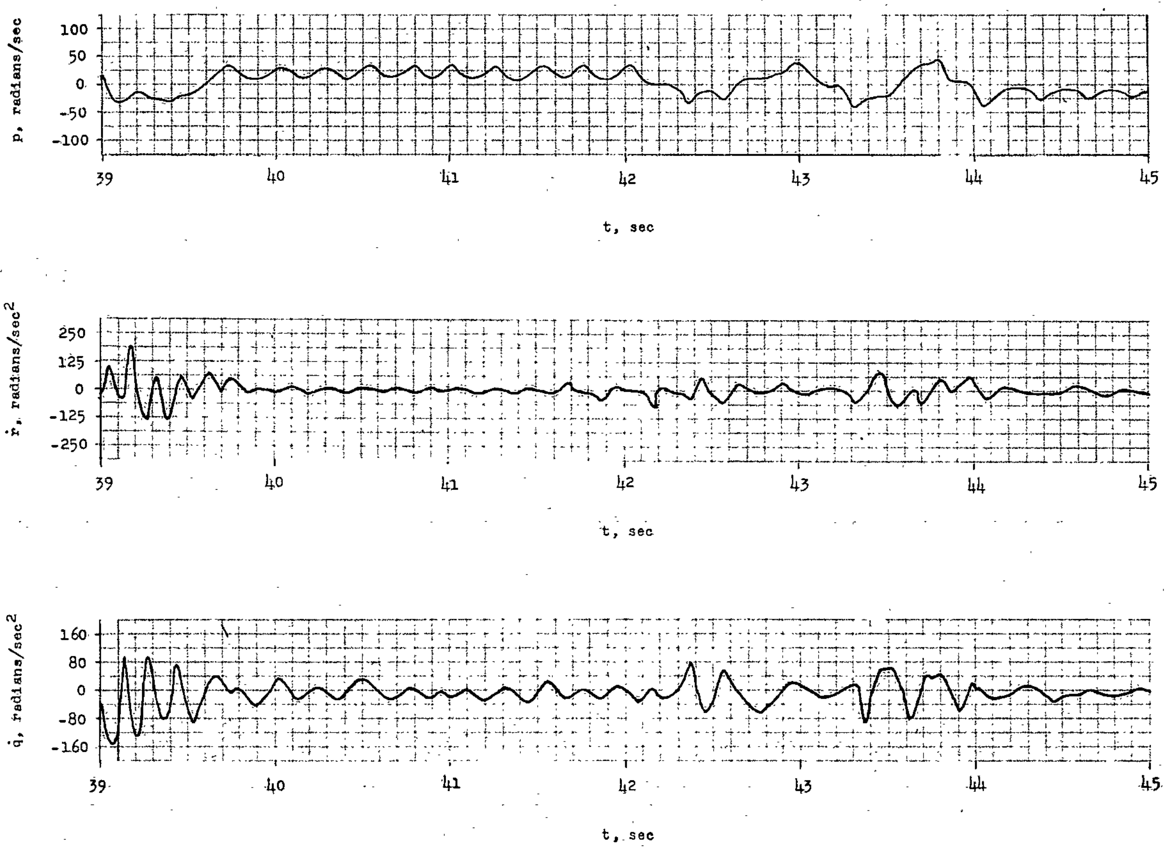

(a) Flight-test motions. Roll rates, angular acceleration in yaw, and angular acceleration in pitch.

Figure 22.- Comparisons of the angular motions obtained from the flight tests and from the analog investigation near Mach number 2.

L-1186

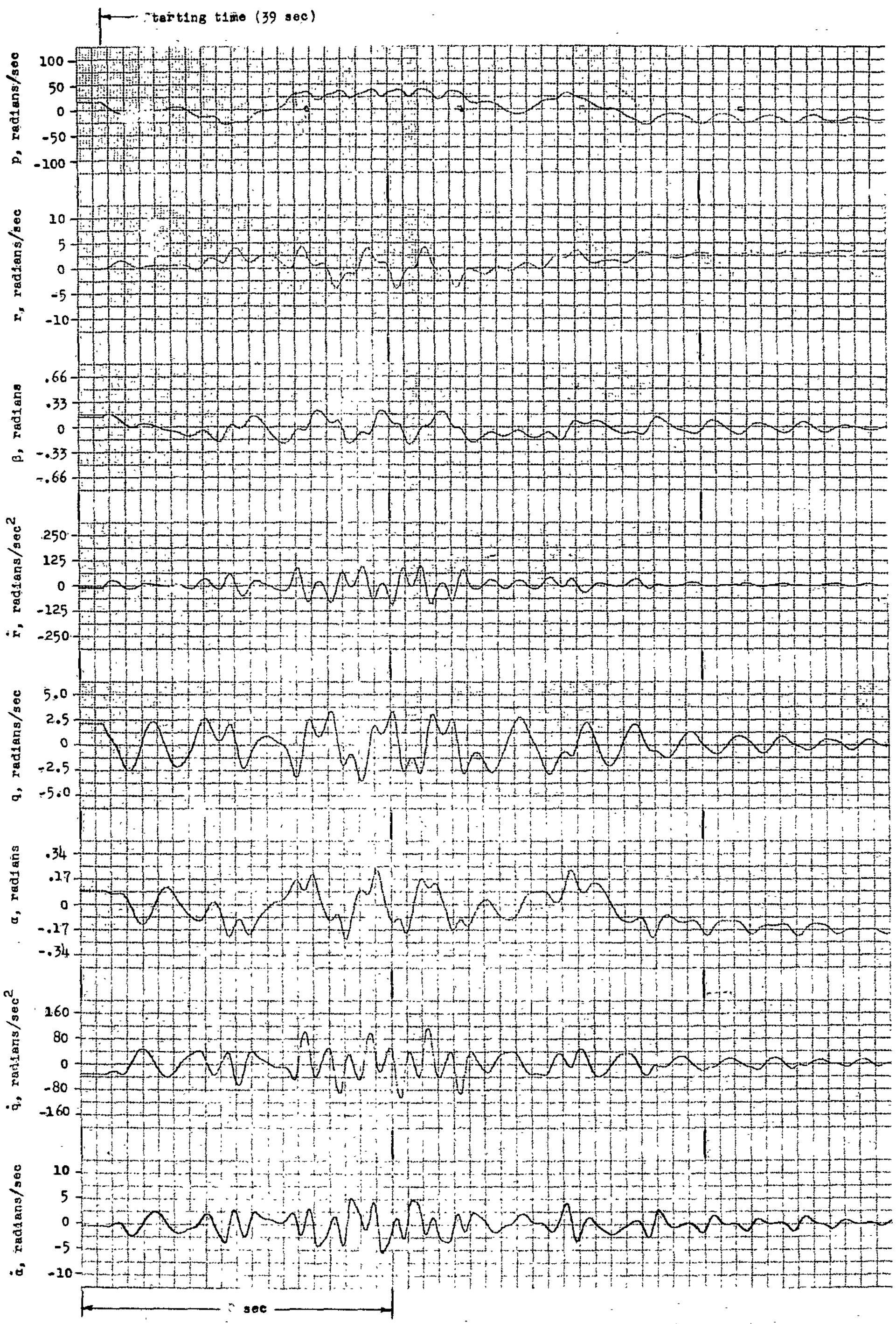

(b) Analog motions. First run.

Figure 22.- Continued.

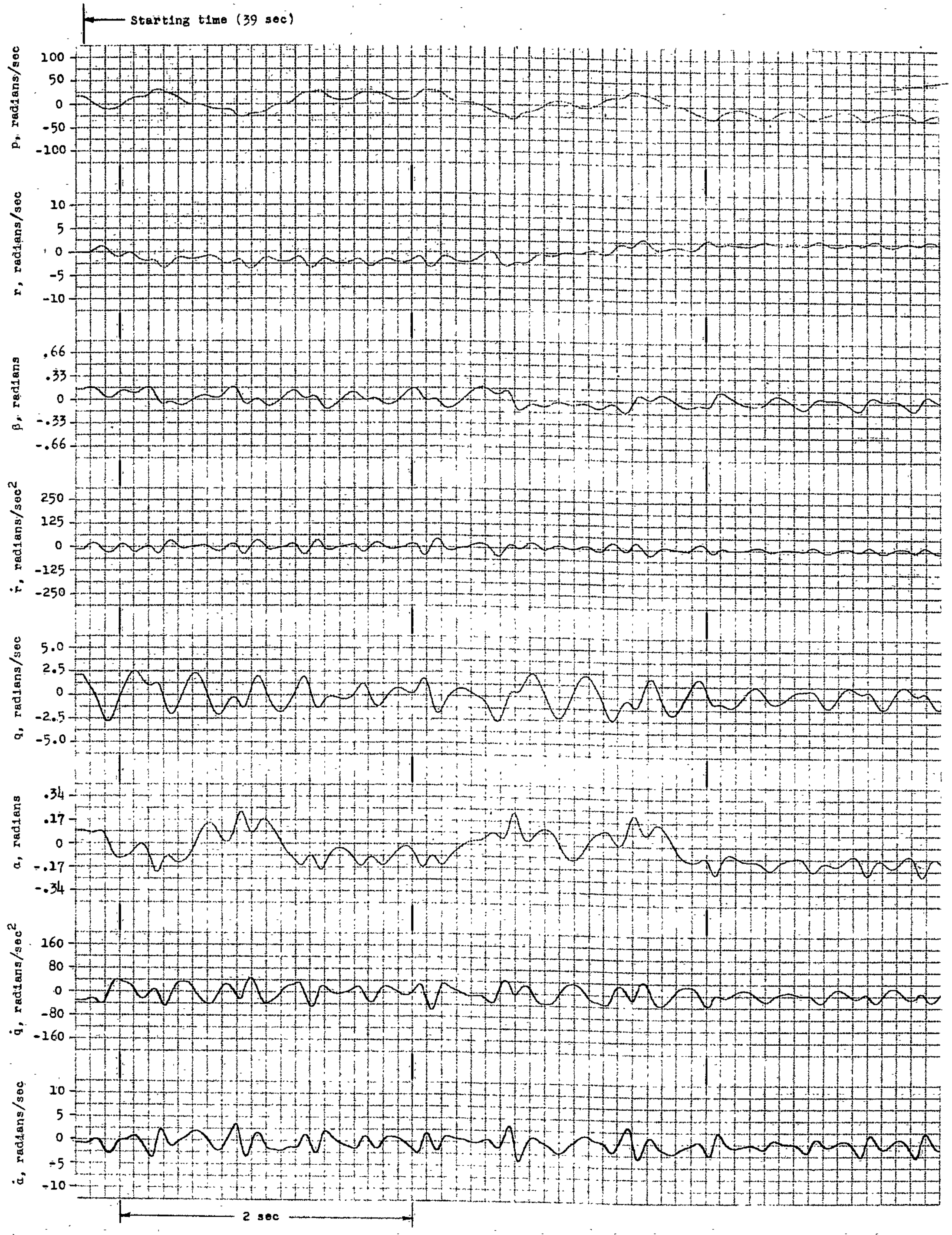

(c) Analog motions. Second run.

Figure 22.- Continued.

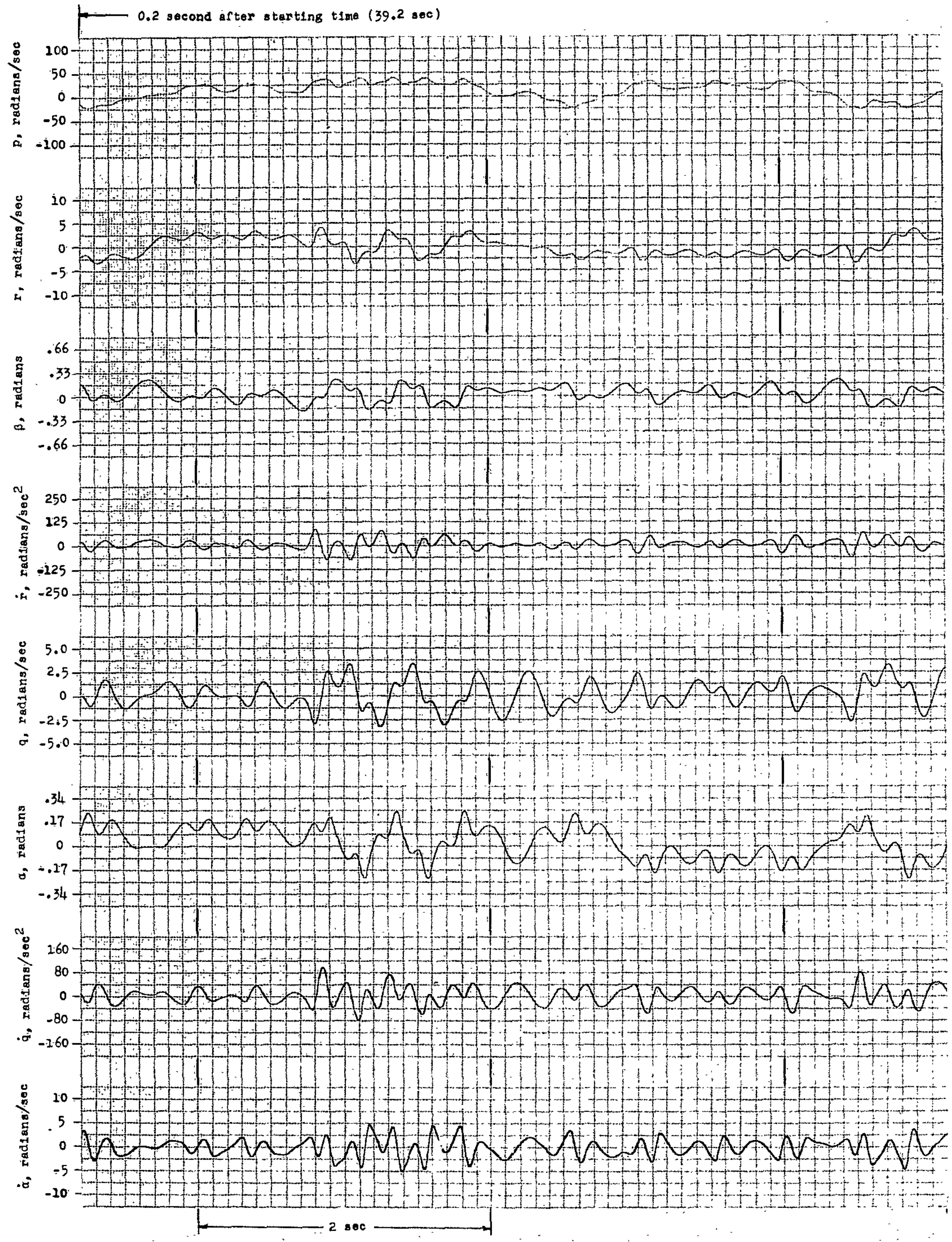

(d) Analog motions. Third run.

Figure 22.- Concluded.

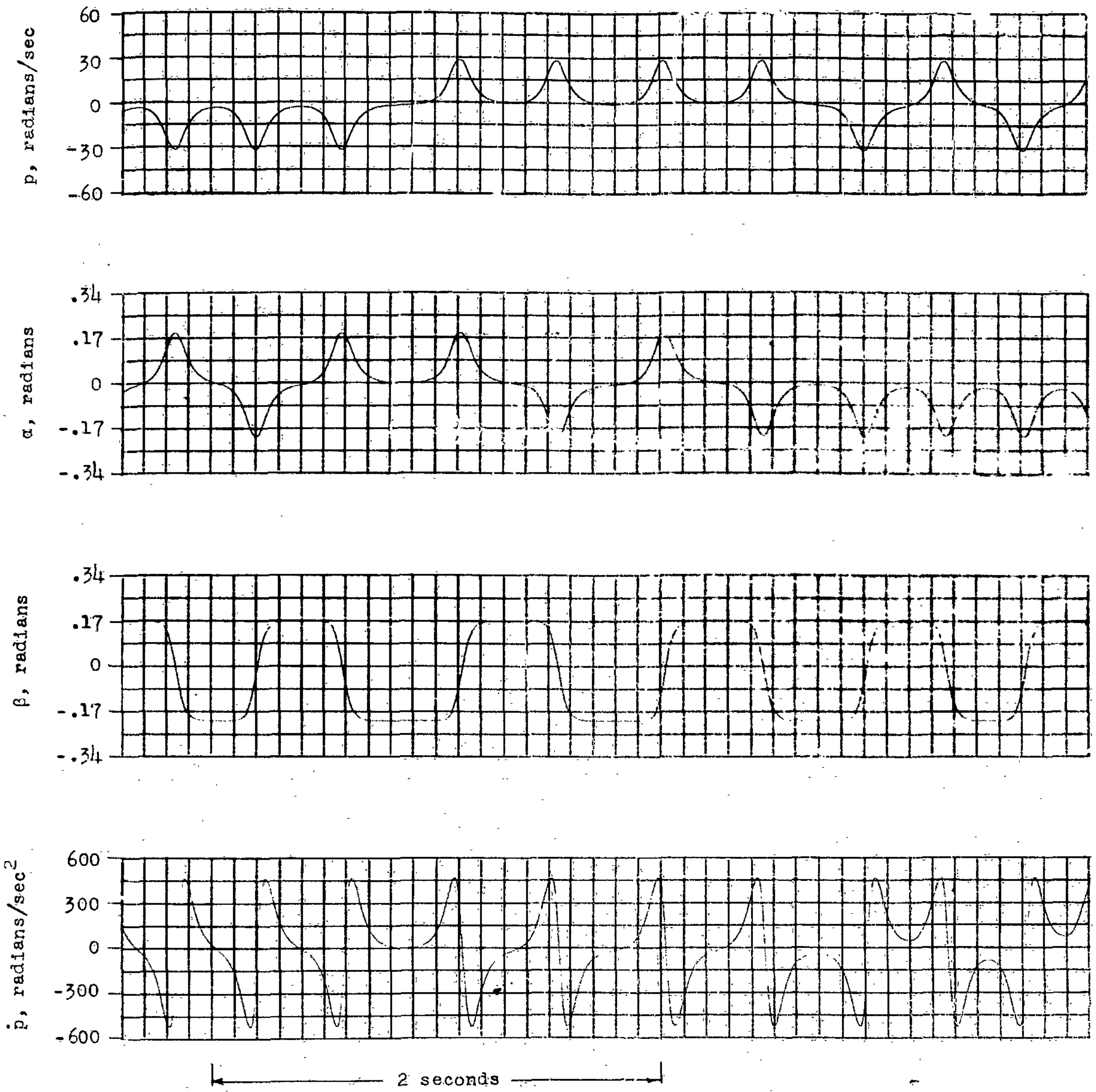

Figure 23.- Angular motions from the simplified equations of motion.

L-1186